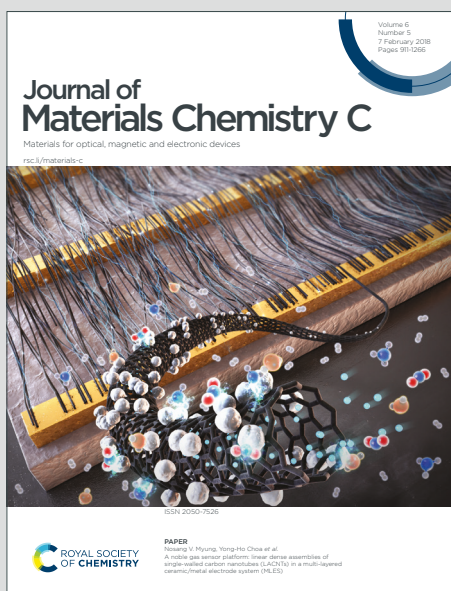


# Journal of Materials Chemistry C

Materials for optical, magnetic and electronic devices

Accepted Manuscript

This article can be cited before page numbers have been issued, to do this please use: J. Yang, Y. Liu, W. Yan, P. Zhou, Z. Wang, Y. Wang, Y. Zhang, Z. Zhang, F. Mo, Z. Ji, H. Haick and Y. Wang, *J. Mater. Chem. C*, 2025, DOI: 10.1039/D5TC01896J.



This is an Accepted Manuscript, which has been through the Royal Society of Chemistry peer review process and has been accepted for publication.

Accepted Manuscripts are published online shortly after acceptance, before technical editing, formatting and proof reading. Using this free service, authors can make their results available to the community, in citable form, before we publish the edited article. We will replace this Accepted Manuscript with the edited and formatted Advance Article as soon as it is available.

You can find more information about Accepted Manuscripts in the [Information for Authors](#).

Please note that technical editing may introduce minor changes to the text and/or graphics, which may alter content. The journal's standard [Terms & Conditions](#) and the [Ethical guidelines](#) still apply. In no event shall the Royal Society of Chemistry be held responsible for any errors or omissions in this Accepted Manuscript or any consequences arising from the use of any information it contains.

1 **Conductive Hydrogel-based Epidermal Electrodes for Electrophysiological**  
2 **Monitoring**

3 *Jiawei Yang<sup>a,b</sup>, Yi Liu<sup>a,b</sup>, Wenqing Yan<sup>a,b</sup>, Pengcheng Zhou<sup>a,b</sup>, Zonglei Wang<sup>a,b</sup>, Yuli*  
4 *Wang<sup>a,b</sup>, Yujie Zhang<sup>a,b</sup>, Zongman Zhang<sup>a,b</sup>, Fan Mo<sup>c</sup>, Zichong Ji<sup>a,b</sup>, Hossam Haick<sup>b</sup>,*  
5 *Yan Wang<sup>a,b,d</sup>\**

6  
7 <sup>a</sup> Department of Chemical Engineering, Guangdong Technion-Israel Institute of  
8 Technology 241 Daxue Road, Shantou, Guangdong 515063, China

9 <sup>b</sup> The Wolfson Department of Chemical Engineering, Technion-Israel Institute of  
10 Technology, Haifa 3200003, Israel

11 <sup>c</sup> Department of Materials Science and Engineering, Technion-Israel Institute of  
12 Technology, Haifa 3200003, Israel

13 <sup>d</sup> Guangdong Provincial Key Laboratory of Materials and Technologies for Energy  
14 Conversion, Guangdong Technion-Israel Institute of Technology, 241 Daxue Road,  
15 Shantou, Guangdong 515063, China

16  
17 **Keywords:** Conductive hydrogels; epidermal electrodes; electrophysiological  
18 monitoring

19

20 **\*E-mail:** wang.yan@technion.ac.il; yan.wang@gtiit.edu.cn



21 **Abstract**

22 Electrophysiological signals generated by human physiological processes offer critical  
23 insights for health monitoring and disease diagnosis, with their precise acquisition  
24 depending on high-performance electrodes. Conductive hydrogel-based epidermal  
25 electrodes, owing to their superior properties, demonstrate significant promise in  
26 electrophysiological monitoring. This review presents a comprehensive summary of the  
27 recent progress in the design and application of conductive hydrogels for epidermal  
28 electrophysiological electrodes. It first categorizes the various types of conductive  
29 hydrogel materials, highlighting recent advancements and their unique advantages as  
30 electrode interfaces. Subsequently, the key properties of conductive hydrogel-based  
31 epidermal electrodes are discussed, including conductivity, adhesion, stretchability, and  
32 gas-permeability. Then, state-of-the-art applications across multiple  
33 electrophysiological domains are introduced, ranging from electrocardiography,  
34 electromyography, electrooculogram, and electroencephalography. Finally, a  
35 conclusion and future directions for the conductive hydrogel-based epidermal  
36 electrodes in electrophysiological monitoring are provided.



## 37 1. Introduction

38 Electrophysiological signals, including electrocardiogram (ECG), electromyogram  
39 (EMG), electroencephalogram (EEG), and electrooculogram (EOG), reflect critical  
40 human physiological processes, capturing bioelectric activity from heartbeats, muscle  
41 contractions, and neural functions<sup>1</sup>. These signals are essential for diagnosing and  
42 monitoring cardiovascular conditions<sup>2, 3</sup>, investigating neurological disorders<sup>4, 5</sup>,  
43 supporting motor rehabilitation<sup>6, 7</sup>, and advancing human-computer interaction  
44 systems<sup>8, 9</sup>. Characterized by high temporal and spatial complexity, these signals exhibit  
45 amplitudes ranging from microvolts to millivolts and frequencies spanning sub-hertz to  
46 hundreds of hertz<sup>10</sup>. Consequently, skin-mountable electrodes, as the cornerstone of  
47 electrophysiological signal acquisition, must combine high sensitivity, mechanical  
48 stability, stretchability, and conformal skin contact to maintain signal fidelity and  
49 improve clinical outcomes<sup>11-15</sup>.

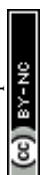
50 Electrodes are generally categorized as invasive or non-invasive and serve as critical  
51 interfaces in biochemical sensing and human health monitoring, enabling efficient  
52 transmission and transduction between biological signals and electronic systems<sup>16-20</sup>.  
53 Invasive electrodes, implanted to directly interface with target tissues, yield high-  
54 resolution signals but are constrained by surgical risks and invasiveness, limiting their  
55 use in routine monitoring. Non-invasive electrodes, which capture signals through skin  
56 contact, are further divided into dry and wet electrodes. Dry electrodes, typically  
57 constructed from metals or rigid conductive materials, are valued for their reusability  
58 and ease of application but exhibit high stiffness, making it challenging to maintain  
59 intimate skin contact during dynamic deformation or movement<sup>21</sup>. This often results in  
60 skin-electrode contact gaps, elevating interface impedance and diminishing the signal-  
61 to-noise ratio (SNR). Wet electrodes, such as commercial Ag/AgCl gel electrodes,  
62 utilize conductive gel to enhance skin-electrode contact for lower skin-electrode  
63 impedance, delivering high-quality signals in the short term<sup>22</sup>. However, they typically



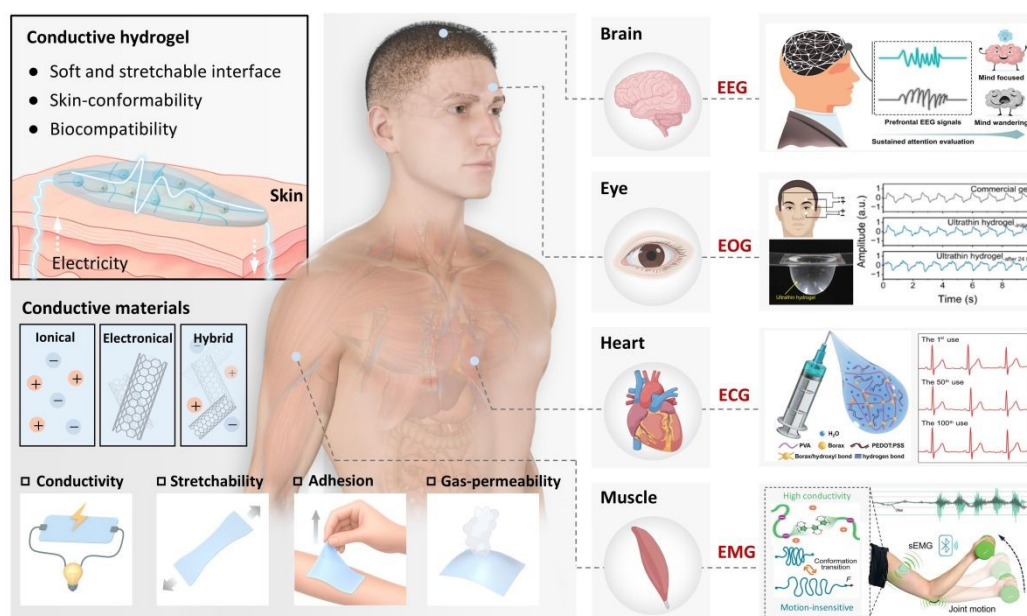
64 rely on semi-liquid conductive gels, prolonged use may lead to discomfort, allergic  
65 reactions, or signal attenuation due to gel desiccation or skin irritation. Moreover, their  
66 rigidity hampers signal acquisition in dynamic settings. In recent years, advancements  
67 in flexible electronics have positioned epidermal electrodes made from flexible  
68 materials as compelling alternatives to conventional electrodes<sup>23-25</sup>. With exceptional  
69 stretchability (exceeding 200% strain), skin-matched low modulus, and ultra-thin  
70 profiles, these electrodes establish soft, stable skin interfaces, markedly reducing skin  
71 contact impedance and enhancing SNR. Consequently, the development of flexible  
72 epidermal electrodes optimized for long-term, stable signal acquisition has emerged as  
73 a pivotal research priority.

74 Hydrogels are hydrophilic, cross-linked polymer networks that stably retain at least 10  
75 wt % water within their three-dimensional structure<sup>26</sup>. This structure imparts  
76 exceptional biocompatibility and a low Young's modulus, rendering hydrogels ideal  
77 for skin-contact applications<sup>27, 28</sup>. Traditional hydrogels generally exhibit poor  
78 electrical conductivity, which impairs their ability to respond to external signals and  
79 restricts their effectiveness in electrophysiological signal acquisition. To address this,  
80 researchers have engineered conductive hydrogels by integrating conductive  
81 elements—such as conductive polymers, nanomaterials, or ions—achieving  
82 remarkable electrical performance<sup>29-35</sup>. Fine-tuning the proportions of these  
83 components enables precise control over hydrogel conductivity. Furthermore, through  
84 innovative structural and chemical designs, conductive hydrogels can exhibit superior  
85 mechanical toughness, high conductivity, self-adhesion, and breathability<sup>36, 37</sup>.

86 In recent years, conductive hydrogels have attracted significant research interest due to  
87 their promising applications in bioelectronics and wearable devices<sup>38-40</sup>. For example,  
88 Mo et al.<sup>41</sup> reviewed recent advancements in ionic conductive hydrogels for skin sensor  
89 applications. While previous reviews have focused on specific subtypes—such as ionic  
90 liquid (IL)-based or nanomaterial-based conductive hydrogels—there remains a lack of  
91 comprehensive discussion on their role as epidermal electrodes for electrophysiological



92 monitoring<sup>25, 42-44</sup>. Ding et al.<sup>45</sup> summarized the progress of conductive hydrogels in  
 93 electrophysiological signal acquisition; however, a holistic review encompassing  
 94 material design, performance requirements, and practical applications in  
 95 electrophysiological monitoring is still lacking. Therefore, this review aims to provide  
 96 a comprehensive overview of the latest research trends in conductive hydrogel-based  
 97 epidermal electrodes for electrophysiological applications. We begin by systematically  
 98 introducing the typical materials used in conductive hydrogels, including design  
 99 strategies for electronically conductive, ionically conductive, and hybrid conductive  
 100 systems. Next, we discuss the key performance requirements for conductive hydrogel  
 101 epidermal electrodes, such as conductivity, adhesion, stretchability, and gas-  
 102 permeability. Finally, we summarize recent advances in their application for monitoring  
 103 various electrophysiological signals (Fig. 1).



104  
 105 **Fig. 1 Schematic interpretation of conductive hydrogel-based epidermal**  
 106 **electrodes for electrophysiological monitoring.** The left side illustrates representative  
 107 types of conductive hydrogel materials, including ionic-based, electronic-based, and  
 108 hybrid-based, along with their key properties, such as electrical conductivity,  
 109 stretchability, adhesion, and gas permeability. The right side exhibits representative  
 110 examples of electrophysiology monitoring, including ECG, EMG, EEG, and EOG.  
 111 Reproduced with permission [46,47]. Copyright 2023, 2025, Wiley-VCH. Reproduced  
 112 with permission [48]. Copyright 2024, Springer Nature. Reproduced with permission  
 113 [49]. Copyright 2024, American Association for the Advancement of Science.



## 114 2. Materials of Conductive Hydrogel-based Epidermal Electrodes

115 Conductive hydrogels are composed of selectively introduced conductive fillers  
116 embedded in a cross-linked hydrophilic polymer matrix. Based on this fabrication  
117 method and configuration, we divide the epidermal electrodes based on conductive  
118 hydrogels into three categories: ionically conductive materials, electronically  
119 conductive materials, and hybrid conductive systems. In this section, we will discuss  
120 the representative materials of these three conductive hydrogel-based epidermal  
121 electrodes.

### 122 2.1 Ionically conductive hydrogel-based epidermal electrodes

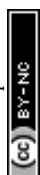
123 Hydrogels, composed of one or more hydrophilic polymers, can absorb and retain  
124 significant amounts of water within their three-dimensional network structure<sup>50</sup>.  
125 Leveraging the intrinsic hydrophilicity of hydrogel networks and the high mobility of  
126 ions in aqueous environments, ionically conductive hydrogels are typically formed by  
127 incorporating mobile ions into a crosslinked, water-rich polymer matrix. These  
128 hydrogels conduct electricity through the transport of ions such as Na<sup>+</sup>, K<sup>+</sup>, and Cl<sup>-</sup>  
129 within the hydrated phase, which serves as the primary conduction medium. Under an  
130 applied electric field, the ions migrate through the network, enabling efficient ionic  
131 conduction<sup>51</sup>. Ion-conductive hydrogels are classified into three typical conductive  
132 mechanisms according to the migration mode of charge carriers and the characteristics  
133 of the conductive path: electrolyte-based, polyelectrolyte-based, and IL-based<sup>52</sup>. In  
134 electrolyte-based hydrogels, ionic conductivity results from the migration of small,  
135 dissociated ions (e.g., Na<sup>+</sup>, Cl<sup>-</sup>) through the water-rich polymer network. These ions—  
136 introduced by dissolving inorganic salts or acids—can migrate freely within the  
137 hydrated phase when an electric field is applied. Electrolyte-based hydrogels are  
138 typically formulated by embedding these electrolytes into the polymer matrix, with  
139 commonly used examples including sodium chloride (NaCl), potassium chloride (KCl),



140 lithium chloride (LiCl), sodium sulfate ( $\text{Na}_2\text{SO}_4$ ), potassium dihydrogen phosphate  
141 ( $\text{KH}_2\text{PO}_4$ ), tetramethylammonium chloride (TMACl), lactic acid, and various citrate  
142 salts<sup>41</sup>.

143 Among typical chlorides, LiCl as a dopant can impart high conductivity to hydrogels,  
144 which significantly reduces skin contact impedance and enables the acquisition of high-  
145 quality biopotential signals. Meanwhile, the introduction of ions can enhance the water  
146 retention of hydrogels, which is crucial for achieving long-term stable monitoring of  
147 biopotential signals<sup>53</sup>. A typical example is that Li et al.<sup>54</sup> designed a body temperature-  
148 triggered adhesive ionic conductive hydrogel based on biocompatible polyacrylamide  
149 (PAM), gelatin, LiCl, and sodium alginate (SA) (PGS hydrogel).  $\text{Li}^+$  can freely shuttle  
150 within the network structure of the PGS hydrogel, and the flow of these ions imparts  
151 conductivity to the hydrogel (Fig. 2a). The conductivity of the PGS hydrogel  
152 significantly increases with increasing LiCl content, rising from  $0.28 \pm 0.01$  to  $5.69 \pm$   
153  $0.20$  S/m (Fig. 2b). Furthermore, the conductivity of the PGS hydrogel remains largely  
154 stable under various stretching conditions (Fig. 2c). Even when the PGS hydrogel is  
155 stretched by 20% strain, the brightness of a light-emitting diode connected to it remains  
156 nearly unchanged. This demonstrates the stable conductivity of the PGS hydrogel in  
157 complex environments, facilitating high-quality electrophysiological monitoring.

158 Polyelectrolytes serving as ionically conductive fillers bear covalently bound ionic  
159 groups (e.g.,  $-\text{COO}^-$ ,  $-\text{SO}_3^-$ ) along the polymer backbone. In polyelectrolyte-based  
160 hydrogels, conductivity arises primarily from the migration of mobile counter-ions (e.g.,  
161  $\text{Na}^+$ ,  $\text{K}^+$ ) via ion hopping and segmental motion within the hydrated network<sup>55, 56</sup>. These  
162 hydrogels offer good mechanical strength, especially in double-network structures, and  
163 their conductivity can be tuned by adjusting polymer concentration, crosslinking  
164 density, and counterion type, making them suitable for hydrated and physiological  
165 conditions. Typical polyelectrolyte fillers in hydrogels include polyacrylic acid (PAA)  
166 and its derivatives, chitosan, SA, etc<sup>52</sup>. Lu et al<sup>57</sup>. developed a double-network (DN)  
167 polyelectrolyte hydrogel, integrating polymer chain entanglement, chemical

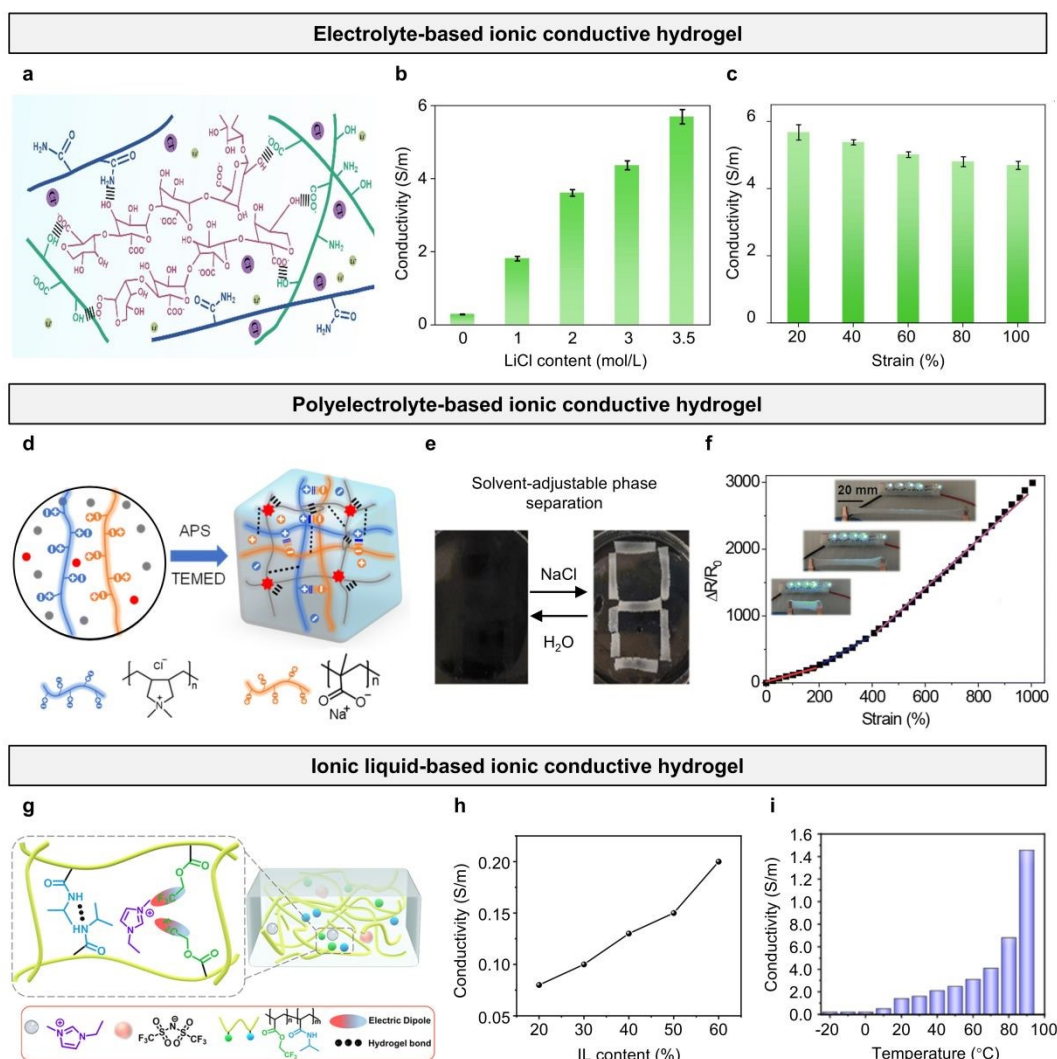




168 crosslinking, and multiple strong and weak intermolecular interactions. The hydrogel  
169 consists of a PAM network and a polyelectrolyte network composed of polyelectrolytes  
170 (poly(diallyldimethylammonium chloride) and poly(diallyldimethylammonium  
171 chloride) (Fig. 2d). The mechanical properties and adhesive strength of polyelectrolyte  
172 DN hydrogels can be customized by modulating the proportions of PAM,  
173 polyelectrolyte, and cosolvent. The optimal formulation yields a tensile modulus of  
174 10.8 kPa, a tensile strain at break of 1000% strain, and an adhesive strength of 37.8 kPa.  
175 Furthermore, the stability of the crosslinked PAM network, combined with the unique  
176 properties of polyelectrolytes that induce phase separation, ensures the hydrogel's  
177 stability even in salt solutions while exhibiting solvent-tunable transparency (Fig. 2e).  
178 Owing to the presence of polyelectrolytes, the hydrogel exhibits excellent conductivity.  
179 This conductive hydrogel can be stretched up to 1100% strain before reaching its  
180 breaking point while maintaining stable conductivity even under high tensile strain (Fig.  
181 2f).

182 IL-based hydrogels incorporate room-temperature ILs—such as 1-ethyl-3-  
183 methylimidazolium bis(trifluoromethanesulfonyl)imide (EMIM-TFSI)—either as co-  
184 solvents or as dispersed conductive media within the hydrogel network. Their ionic  
185 conductivity stems from the unrestricted movement of both organic cations and anions,  
186 which act as charge carriers. These hydrogels exhibit high and humidity-independent  
187 ionic conductivity, excellent electrochemical stability, and strong anti-freezing and  
188 anti-drying properties. They are particularly suitable for long-term use in harsh  
189 environments and maintain good flexibility and thermal stability<sup>58, 59</sup>. By polymerizing  
190 IL monomers into PIL, the inherent properties of IL can be transferred to the polymer  
191 chain, thereby obtaining ionic conductive hydrogels with high conductivity. Zhao et  
192 al.<sup>60</sup> prepared an ionic gel through one-step photoinitiated polymerization of 2,2,2-  
193 trifluoroethyl acrylate and N-isopropylacrylamide (NIPAm) in the hydrophobic ILs 1-  
194 ethyl-3-methylimidazolium bis(trifluoromethylsulfonyl)imide ([EMIm][TFSI]) (Fig.  
195 2g). The ionic gel demonstrates exceptional transparency (94.8%), underwater self-



196 healing capability (up to 96%), toughness (3.93 MJ/m<sup>3</sup>), andView Article Online  
DOI: 10.1039/D5TC01896J

197

198 **Fig. 2 Ionically conductive hydrogel-based epidermal electrodes.** (a) PGS

199 conductive hydrogel and its network structure. (b) Conductivity of PGS hydrogels with

200 different LiCl contents. (c) Conductivity of PGS hydrogel under different strain.

201 Reproduced with permission [54]. Copyright 2024, Elsevier. (d) Schematic diagram of the

202 polyelectrolyte hydrogel preparation and structure. (e) The photograph illustrates the

203 solvent-tunable transparency of the hydrogel electrolyte under induced phase

204 separation. (f) Tensile strain induced relative resistance changes of the hydrogel.

205 Reproduced with permission [57]. Copyright 2025, Royal Society of Chemistry. (g)

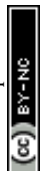
206 Schematic diagram of the structure of the ionogel. (h) Conductivity of ionogel with

207 different IL contents. (i) The ionic conductivities of the ionogel in the temperature

208 range from -20 to 90 °C. Reproduced with permission [60]. Copyright 2023, American

209 Chemical Society.

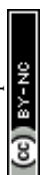
210 underwater adhesion strength (102.77 ± 2.4 kPa). As the ILs mass percentage increased

211 from 20% to 60%, the ionic gel's conductivity surged from 8.15 × 10<sup>-4</sup> to 2.04 × 10<sup>-3</sup>

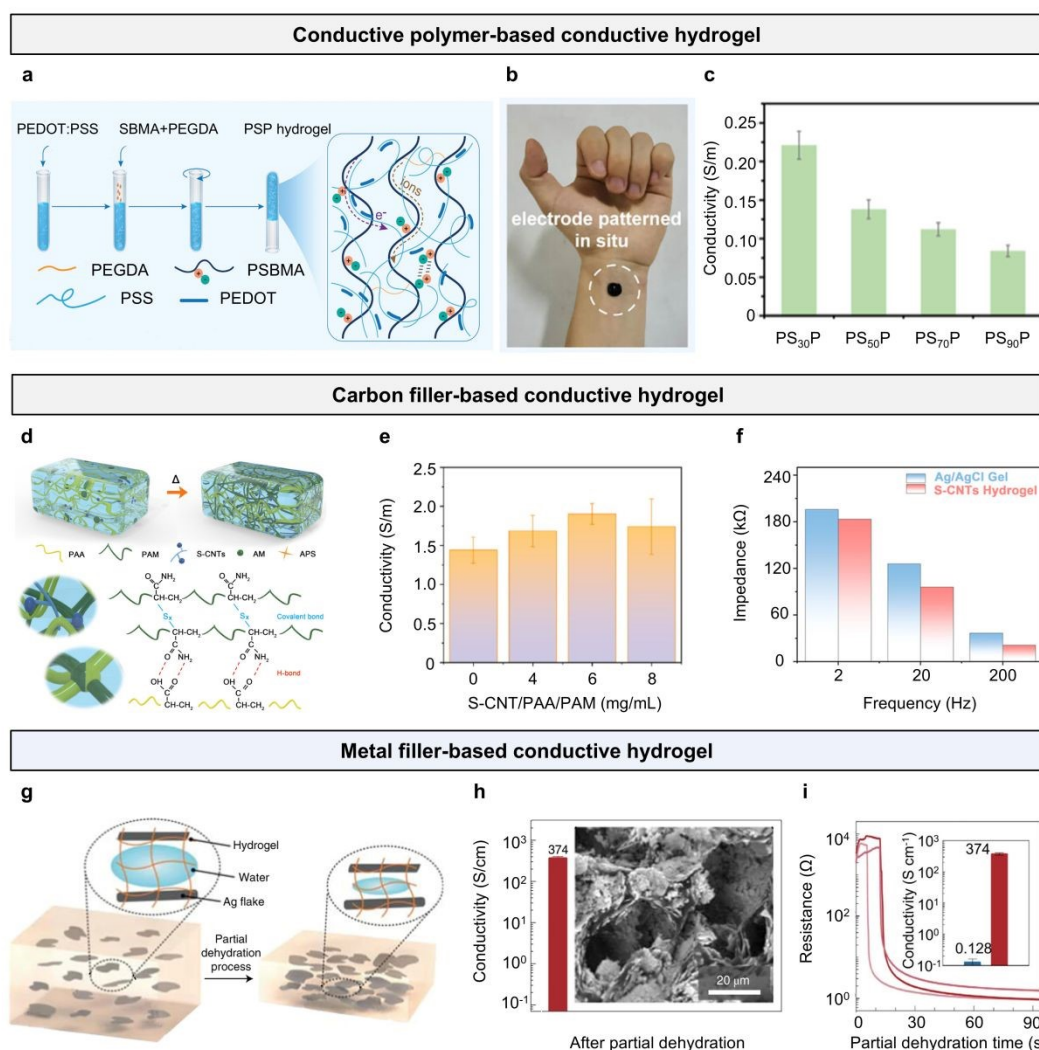
212 S/cm (Fig. 2h). Inspired by the excellent temperature responsiveness of IEs, the  
213 temperature sensitivity of the ionic gel was further characterized. Across a wide  
214 temperature range of  $-20$  to  $90$  °C, the ionic gel exhibited high ionic conductivity ( $2 \times$   
215  $10^{-4}$  to  $1.45 \times 10^{-2}$  S/cm). Due to increased ion mobility, the ionic conductivity sharply  
216 increased with rising temperature (Fig. 2i).

## 217 2.2 Electronically conductive hydrogel-based epidermal electrodes

218 In electronically conductive hydrogel-based epidermal electrodes, the hydrogel matrix  
219 provides a soft, biocompatible scaffold, while embedded conductive materials enable  
220 efficient electron transport. Electrical conduction is achieved by incorporating  
221 intrinsically conductive components into the hydrogel network. These materials form  
222 continuous pathways that support charge transport through electron hopping or band-  
223 like conduction. The conductivity depends on factors such as filler dispersion and  
224 connectivity, polymer crystallinity, doping level, and interfacial interactions<sup>61, 62</sup>.  
225 Electron conduction primarily encompasses three categories: i) conductive polymers,  
226 including poly(3,4-ethylenedioxythiophene) polystyrene sulfonate (PEDOT:PSS),  
227 polypyrrole (PPy), and polyaniline (PANI)<sup>63, 64</sup>; ii) carbon filler-based nanomaterials,  
228 such as carbon nanotubes (CNTs) and graphene oxide (GO)<sup>65, 66</sup>; and iii) metal-filler  
229 nanoparticles, such as silver nanoparticles (AgNPs)<sup>67, 68</sup>. Incorporating these materials  
230 into hydrogels yields electron-conductive hydrogels with enhanced performance. A  
231 typical example is that Huang et al.<sup>69</sup> utilized PEDOT:PSS to promote the self-  
232 polymerization of zwitterionic [2-(methacryloyloxy)ethyl]dimethyl-(3-sulfopropyl)  
233 (SBMA), proposing an in-situ formed conductive hydrogel (PSP) (Fig. 3a). This  
234 hydrogel exhibits exceptional elasticity (elastic recovery rate  $> 96\%$ ), robust adhesion  
235 strength (6.5 kPa), biocompatibility, and intrinsic antibacterial properties. The gelation  
236 process generates minimal heat ( $< 5$  °C), enabling in-situ formation on the skin.  
237 Furthermore, the hydrogel achieves intimate skin contact, creating a highly conformal  
238 interface (Fig. 3b). The PSP hydrogel exhibits high conductivity, attributed to its



239 polycrystalline ionic network and conductive PEDOT:PSS. As the SBMA content  
 240 increases, electronic conductivity of the PSP hydrogel decreases from 0.08 to 0.03 S/m,



241  
 242 **Fig. 3 Electronically conductive hydrogel-based epidermal electrodes.** (a)  
 243 Schematic diagram of the fabrication and promising applications of PSP hydrogel. (b)  
 244 Photographs shows that the PSP hydrogel can be patterned on skin in situ. (c) The  
 245 conductivity of the PSP hydrogel with different SBMA content. Reproduced with  
 246 permission [69]. Copyright 2023, Wiley-VCH. (d) Schematic illustration of the  
 247 preparation process of the S-CNTs/PAA/PAM hydrogel. (e) Conductivity of the  
 248 prepared hydrogel with different S-CNTs content. (f) Impedance comparison at various  
 249 frequencies of the S-CNTs/PAA/PAM hydrogel and commercial Ag/AgCl gel  
 250 electrodes. Reproduced with permission [70]. Copyright 2025, American Chemical  
 251 Society. (g) Composition of the conductive hydrogel composite composed of  
 252 micrometre-scale Ag flakes and PAM-alginate hydrogel (Ag-hydrogel composite). (h)  
 253 Conductivity of the Ag-hydrogel composite after the controlled partial dehydration  
 254 process. (i) Conductivity of the Ag-hydrogel composite and micrographs of the  
 255 composite after the controlled partial dehydration process. Reproduced with permission



256 [71]. Copyright 2021, Nature Publishing Group.  
257 respectively. This reduction is attributed to the higher solid content and intensified  
258 inter- and intra-chain electrostatic interactions, which impede the formation of efficient  
259 conductive pathways. Nevertheless, the PSP hydrogel retains high conductivity, fully  
260 meeting the requirements for EMG monitoring (Fig. 3c).

261 Dai et al.<sup>70</sup> developed a hydrogel-based epidermal electrode composed of graphene  
262 nanoplates, PAA, and PAM (S-CNTs/PAA/PAM). S-CNTs, enriched with graphene  
263 nanoplates, are synthesized via a two-step sulphuration process employing thiourea and  
264 dibenzyl disulfide (Fig. 3d). The incorporation of sulfur atoms strengthens the  
265 interfacial interactions between S-CNTs and PAA/PAM through C–S covalent bonding,  
266 significantly improving the hydrogel's mechanical performance (> 1200% strain) and  
267 electrical conductivity (1.9 S/m). The incorporation of S-CNTs enhances the  
268 conductivity of PAA/PAM hydrogels to a certain extent. The 6S-CNTs/PAA/PAM  
269 hydrogel exhibits a conductivity of 1.9 S/m, surpassing that of the pristine PAA/PAM  
270 hydrogel (1.44 S/m). The unique chain structure of S-CNTs on the polymer chains  
271 shortens the charge migration pathway, thereby increasing the migration rate and  
272 improving conductivity. However, excessive addition of S-CNTs leads to their  
273 aggregation, which increases the overall resistance of the hydrogel and results in  
274 reduced conductivity (Fig. 3e). Moreover, the S-CNTs/PAA/PAM hydrogel, employed  
275 as an epidermal electrode for electrophysiological signal acquisition, demonstrates  
276 significantly lower skin-contact impedance than commercial Ag/AgCl gel electrodes  
277 across the 1–10<sup>5</sup> Hz range (Fig. 3f).

278 Yunsik et al.<sup>71</sup> designed a highly conductive, flexible hydrogel-based epidermal  
279 electrode by embedding micron-scale Ag particles within a PAM-alginate hydrogel  
280 matrix. A critical step in achieving high conductivity involves partial dehydration of  
281 the hydrogel matrix, facilitating the formation of percolation pathways by Ag flakes.  
282 Prior to partial dehydration, the Ag-hydrogel composite exhibits ionic conductivity  
283 with a low conductivity of ~0.13 S/cm. At this stage of the fabrication process, the  
284 volume fraction of Ag fillers (5 vol%) is insufficient to achieve percolation.

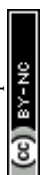
View Article Online  
DOI: 10.1039/D5TC01896J



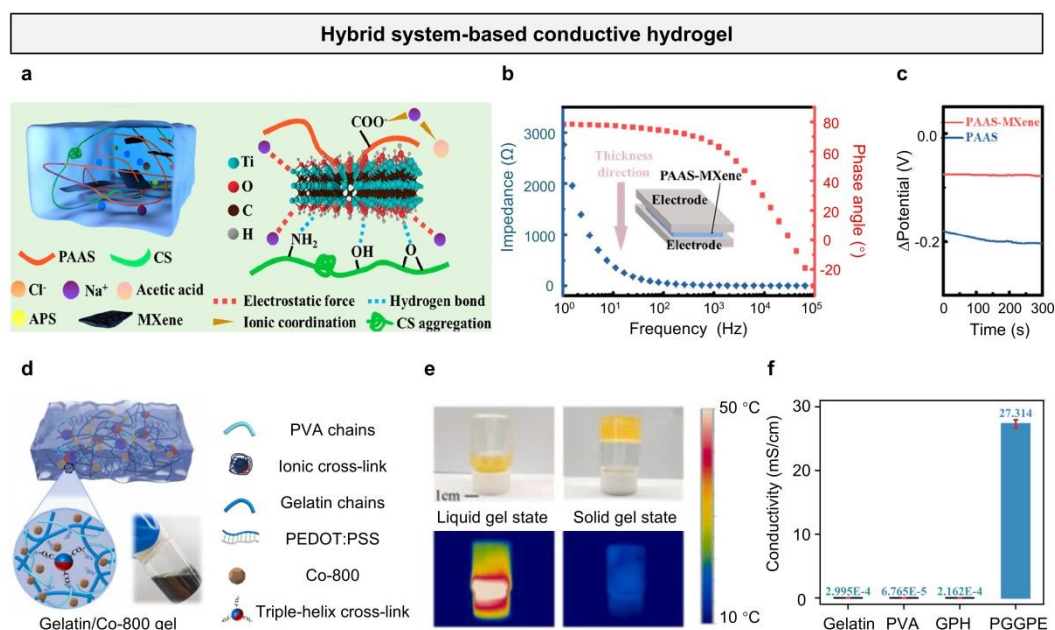
285 Subsequently, the conductivity of the composite increases significantly from 0.12 to  
286 374 S/cm following dehydration (Fig. 3h). During the partial dehydration process, Ag-  
287 hydrogel composites with varying amounts of Ag added in-situ yielded the resistance  
288 values of the hydrogel. The resistance of the Ag-hydrogel composite decreased  
289 exponentially after drying for 10–15 minutes, stabilizing at  $1.14 \pm 0.35 \Omega$  after 90  
290 minutes, with a corresponding volume conductivity of  $374 \pm 30.8$  S/cm (Fig. 3i).

### 291 2.3 Hybrid conductive hydrogel-based epidermal electrodes

292 Hybrid conductive hydrogels combine ionic and electronic conductive components  
293 within a single network, effectively addressing the limitations of pure systems.  
294 Ionically conductive hydrogels offer good biocompatibility and flexibility but often  
295 exhibit reduced conductivity under low humidity or freezing conditions. In contrast,  
296 electronically conductive hydrogels provide stable and high conductivity but may  
297 compromise stretchability and lack sufficient ionic transport. By integrating both  
298 mechanisms, hybrid hydrogels form synergistic, bicontinuous ion–electron conduction  
299 networks that enhance charge transport kinetics and conductivity stability. This dual-  
300 conduction design enables the hydrogel to maintain performance under mechanical  
301 deformation, temperature variation, and environmental stress. Additionally, hybrid  
302 networks allow tunable physical and electrical properties through molecular and  
303 structural engineering, such as tailoring polymer composition, conductive filler  
304 distribution, or crosslinking strategies<sup>72</sup>. For example, Luo et al.<sup>73</sup> designed an MXene-  
305 induced crosslinking fast-gelling hybrid conductive hydrogel electrode (PAAS)  
306 composed of acrylamide, NaCl, and MXene (Fig. 4a). Under the initiation of  
307 ammonium persulfate (APS), the C=C bonds of sodium acrylate are opened for  
308 polymerization, and then MXene acts as a crosslinker to rapidly form polymer chains.  
309 Meanwhile, the introduction of MXene increases the hydrogel's conductivity (2.3 S/m).  
310 In this system, sodium ions from NaCl and poly (sodium acrylate) impart ionic  
311 conductivity to hydrogel, while also establishing electrostatic interactions with MXene



312 and forming ionic coordination with acetic acid used for dissolving chitosan. Due to the  
 313 addition of negatively charged MXene, the directional alignment of positively charged  
 314 chitosan and sodium ions under an external electric field is restricted, reducing the  
 315 hydrogel's polarization potential (change rate less than  $6.5 \times 10^{-4}$  V/min) (Fig. 4b and  
 316 c).



317 **Fig. 4 Hybrid conductive-based conductive hydrogel.** (a) Composition of PAAS-  
 318 MXene cross-linked by single-layer MXene. (b) Electrical impedance of Bode plot in  
 319 the thickness direction of PAAS-MXene hydrogel. (c) Comparison of polarization  
 320 potential values and polarization potential change values of PAAS and PAAS-MXene.  
 321 Reproduced with permission [73]. Copyright 2022, American Chemical Society. (d)  
 322 Schematic illustration of the multifunctional bio-hydrogel. (e) Conductivity of gelatin,  
 323 PVA, GPH, and PEDOT:PSS/graphene/gelatin/PVA hydrogel. (f) Comparison of  
 324 single heartbeat waveform recorded by hydrogel electrode and commercial electrode.  
 325 Reproduced with permission [74]. Copyright 2023, Wiley-VCH.

327 Wang et al.<sup>75</sup> developed a hybrid conductive hydrogel leveraging the synergistic effects  
 328 of PEDOT:PSS/graphene and Na<sup>+</sup> ions (Fig. 4d). The hydrogel (GPH), composed of a  
 329 dual-crosslinked network of gelatin and polyvinyl alcohol (PVA), exhibits a unique  
 330 thermally responsive reversible phase transition between a flowable fluid state and a  
 331 viscoelastic gel state (Fig. 4e). Compared to pristine hydrogels ( $6.76 \times 10^{-5}$  mS/cm),  
 332 the conjugated structure of PEDOT:PSS in the hybrid conductive hydrogel facilitates  
 333 electron mobility, while graphene sheets form a conductive network that supports



334 efficient electron and ion transport. This results in significantly enhanced electrical  
335 conductivity, reaching 27.31 S/cm (Fig. 4f).

### 336 3. Properties of Conductive Hydrogel-based Epidermal Electrodes

337 To fulfill the essential requirements for electrophysiological signal monitoring,  
338 conductive hydrogel-based epidermal electrodes can be engineered with tailored  
339 properties, including conductivity, stretchability, and adhesion, using diverse synthesis  
340 and fabrication techniques (Table 1). This section outlines the essential properties  
341 required for conductive hydrogel epidermal electrodes, highlighting their critical role  
342 in ensuring the efficacy and reliability of electrophysiological monitoring.

343 **Table 1 Summary of conductive hydrogel-based epidermal electrodes from**  
344 **different conductive mechanisms.**

Conductive types	Hydrogel matrix	Conductivity materials	Conductivity (Test method)	Stretchability (%)	Adhesion (kPa)	Biocompatibility	Electrophysiological signals	Ref.
Ionic	AM/BIS/Water	NaCl	1.3 S/m (EIS)	1326	14	-	ECG/EEG	76
	AAM/PEGDA/Water	LiCl	0.01 S/m (EIS)	2500	-	-	EOG/EEG	77
	PVA/b-PEI/Water	CaCl <sub>2</sub>	3.09 S/m (EIS)	1291	10	-	ECG/EMG/EEG	78
	EGDMA/Water	VBIm-NTF <sub>2</sub>	0.0065 S/m (AC Resistance)	200	~400	-	ECG	79
	HEMA/SBMA/MBA/Water	LiTFSI	3 S/m (Four-point Probe)	287	7.5	High	ECG/EMG	80
	PAM/PDDA/Water	PMAANa	-	1000	19.2	-	ECG/EMG	57
	DMAEA/MBA/KPS/Water	ZM	-	1880	400	High	ECG/EMG	81
	AAM/LMA/KPS/Water	-	-	1410	-	High	ECG/EMG	82
	PVA/PAM/F-SiO <sub>2</sub> /Water	CaCl <sub>2</sub>	10.58 S/m (EIS)	1450	26	-	ECG/EMG	83
	Gelatin glycerol/Borax/Water	Na <sub>2</sub> SO <sub>4</sub>	9.3 S/m (EIS)	696	176	-	ECG/EMG/EEG/EOG	49
	Proanthocyanins/Guar gum/CNF/Water	FeCl <sub>3</sub>	0.023 S/m (Four-point Probe)	-	7.9	-	ECG/EMG	84
EG/AAm/MBA/Water	DES	1.6 S/m (AC Resistance)	1660	0.01	High	ECG/EMG	85	
Electronic	PVA/PDA/Water	PEDOT:PSS	2.18 S/m (Four-point Probe)	535	197	-	EMG	86
	PDA/Water	PEDOT:PSS	4 S/m (AC Resistance)	1300	22.4	High	ECG/EMG	87
	PVA/SA/APS/FeCl <sub>3</sub> /Water	PEDOT:PSS	0.256 S/m (EIS)	334	-	-	ECG/EMG/EEG	88
	NIPAm/HEA/Water	poly(Cu-arylacetylde)	3.1 S/m (EIS)	108	43	High	ECG/EMG	89
	APS/SA/MBAA/KCl/CaSO <sub>4</sub> /Water	PEDOT:PSS	-	50	64	High	EEG	90
	PAM/AM/Silk fibroin/Water	MXene	0.25 S/m (AC Resistance)	1560	29	-	EMG/EOG	91
	TA/ACC/Water	LM	0.02 S/m (EIS)	1000	28.9	High	ECG/EMG	92
	PVA/Borax/Water	PEDOT:PSS	0.002 S/m (Two-point Probe)	10000	15.7	-	ECG/EMG	93
	PAA/AlNO <sub>3</sub> /Water	MXene	0.7 S/m	2400	494.2	-	ECG/EMG	94
	PAA/PVA/Water	RGO	0.11 S/m (Two-point Probe)	-	5.4	High	ECG/EMG/EOG	95
PAM/Alginate/Water	Ag	37400 S/m (Four-point Probe)	250	-	-	EMG	71	
Hybrid	PEGDA/Water	PEDOT:PSS/SBMA	0.03 S/m (EIS and DC Resistance)	390	6.5	High	ECG/EMG	69
	PAA/SA/AD/ADQ/Water	MXene/LiCl	1.8 S/m (EIS)	800	~27	High	ECG	96
	HA/Water/Glycerin	GNs/KCl/NaCl	0.33 S/m (EIS)	-	~5.5	High	EEG	97
	PEDOT:PSS/Fe/Water	PEDOT:PSS/Fe	1.25 S/m (EIS)	15	-	High	ECG	98
	PAA/TOCNFs/Water	PEDOT:PSS/Al(TFSI) <sub>3</sub>	7.1 S/m (EIS)	770	28	High	ECG/EMG	99
	PVA/Water	PPy/FeCl <sub>3</sub>	80 S/cm (Four-point Probe)	36	-	High	EMG	100

345 BIS: N,N'-Methylenebisacrylamide; PEGDA: poly(ethylene glycol) diacrylate; HEMA: 2-  
346 Hydroxyethyl methacrylate; SBMA: [2-(Methacryloxy) ethyl] dimethyl-(3-sulfo-propyl) ammonium





347 hydroxide; MBA: N,N'-Methylenebisacrylamide; SBMA: zwitterionic [2-  
348 (methacryloyloxy)ethyl]dimethyl-(3-sulfopropyl); LiTFSI: bistrifluoromethanesulfonimide lithium  
349 salt; PDA: polydopamine; NIPAm: N-isopropylacrylamide; HEA: 2-hydroxyethyl acrylate; GNs:  
350 graphite nanoparticles; HA: hyaluronic acid; DMAEA: 2-(Dimethylamino) ethyl acrylate; MBA:  
351 N,N'-methylenebis(acrylamide); KPS: potassium persulfate; LMA: lauryl methacrylate; ACC:  
352 calcium carbonate. EIS: electrochemical impedance spectroscopy.

### 353 3.1 Conductivity

354 The conductivity of hydrogel-based epidermal electrodes significantly influences the  
355 performance of bioelectronic interface electrodes, crucial for enabling efficient  
356 electrical signal transmission between biological tissues and electronic components  
357 while ensuring stable electrophysiological communication<sup>101</sup>. The polymer network  
358 serves as a structural scaffold, while the conductive fillers confer electrical conductivity  
359 to the hydrogel<sup>32, 102</sup>. To date, a range of conductive materials, encompassing both  
360 electronic and ionic conductive fillers, have been employed in the fabrication of  
361 conductive hydrogels for epidermal electrodes<sup>102</sup>.

362 Ionic conductive fillers are incorporated into hydrogel systems by introducing acids  
363 (e.g., HCl, H<sub>2</sub>O<sub>4</sub>, H<sub>3</sub>O<sub>4</sub>, ionic compounds (e.g., LiCl, FeCl<sub>3</sub>, AlCl<sub>3</sub>, NaOH, KOH), or  
364 ionic liquids (e.g., 1-ethyl-3-methylimidazolium sulfate), which release free ions to  
365 significantly enhance electrical conductivity<sup>41, 103</sup>. For instance, Zhang et al.<sup>104</sup> prepared  
366 highly conductive hydrogels by adding KOH and NaOH to a carboxymethyl chitosan  
367 (CECT)/PAM-based hydrogel (CTA). The ionic conductivity of the hydrogel samples  
368 was measured using electrochemical impedance spectroscopy, with conductivity  
369 ranging from 0.38 to 0.62 S/m.

370 Another way to achieve high conductive performance is typically to incorporate  
371 electronic conductive fillers (such as intrinsically conductive polymers, metal  
372 nanoparticles, or carbon-based nanomaterials) into hydrogels<sup>105, 106</sup>. A typical example  
373 is that Wang et al.<sup>107</sup> employed a synergistic approach combining freeze-drying and

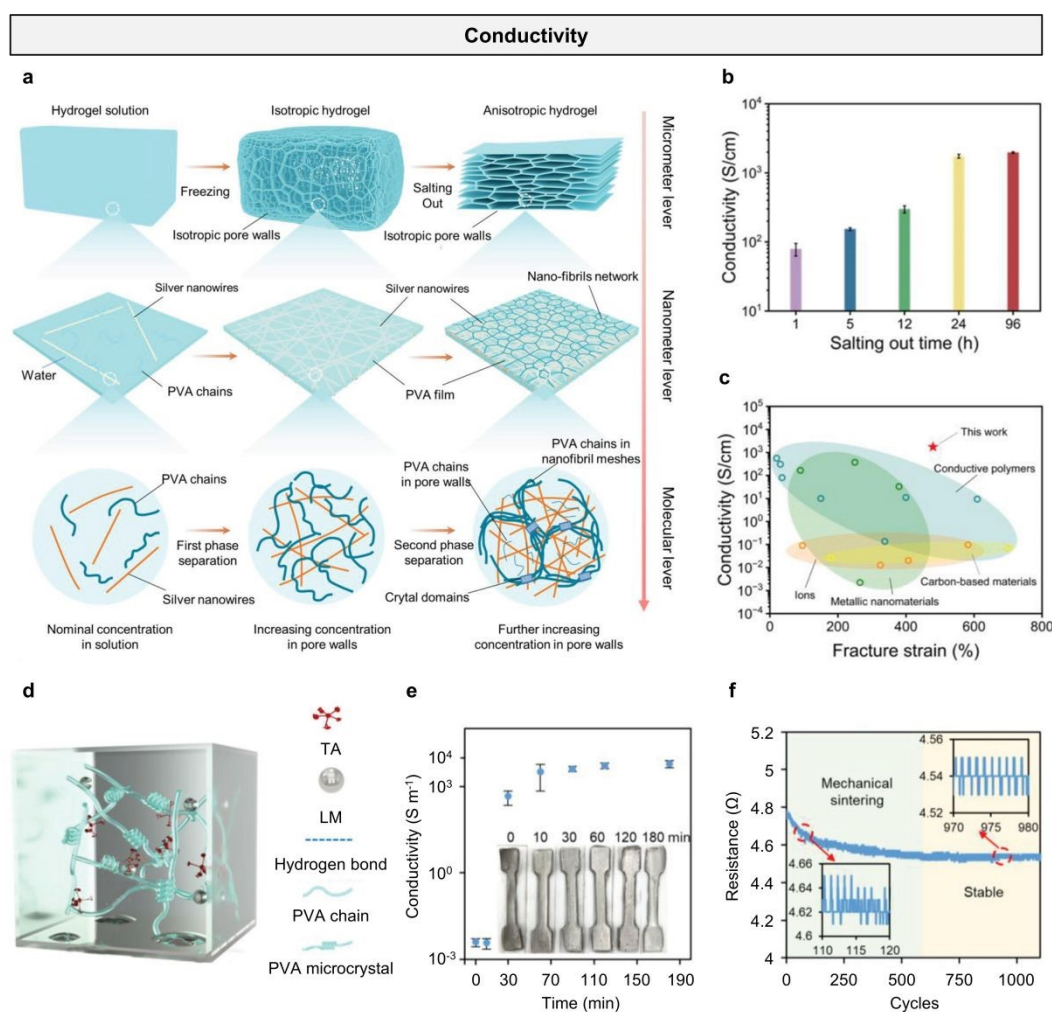


374 salting-out treatment to prepare a conductive hydrogel composite based on silver  
375 nanowires (AgNWs) and PVA (Fig. 5a). This method successfully constructed a  
376 layered hydrogel structure and significantly enhanced the local concentration of  
377 AgNWs by inducing continuous phase separation. The resulting conductive hydrogel  
378 composite exhibited remarkable properties, including ultra-high conductivity, excellent  
379 stretchability (480% strain), and outstanding biocompatibility. The phase separation of  
380 PVA in the hydrogel evolves with the extension of the salting-out time. By optimizing  
381 the salting-out treatment time, the researchers successfully controlled the phase  
382 separation process, resulting in a hydrogel with a conductivity exceeding 1739 S/cm  
383 (Fig. 5b). Due to the high concentration of AgNWs, the prepared hydrogel still  
384 maintains high conductivity under stretching, which is superior to other types of  
385 hydrogels (Fig. 5c). Zhang et al.<sup>108</sup> developed a liquid metal (LM)-doped PVA-LM  
386 hydrogel, incorporating LM microdroplets within a tannic acid (TA)-modified PVA  
387 matrix (Fig. 5d). LM microdroplets were employed as crosslinkers to enhance  
388 mechanical properties while providing exceptional conductivity, reaching a peak value  
389 of 217895 S/m. The sedimentation time of LM profoundly influences the hydrogel's  
390 conductivity, with the non-sedimented PVA-LM hydrogel exhibiting a significantly  
391 lower conductivity of 0.004 S/m. After a sedimentation time of 30 minutes, the  
392 conductivity of the PVA-LM hydrogel surged by five orders of magnitude to 455 S/m,  
393 reflecting significant LM microdroplet precipitation (Fig. 5e). The PVA-LM hydrogel  
394 was subjected to resistance measurements over 1200 stretching cycles (40% strain),  
395 during which its resistance progressively decreased from 4.8 to 4.5  $\Omega$  (Fig. 5f). This  
396 suggests mechanical sintering of LM microdroplets on the hydrogel surface under  
397 external forces, concurrently enhancing its conductivity.

398 For epidermal electrodes, both ionic and electronic conductivity are essential yet  
399 functionally distinct. Ionic conductivity plays a crucial role in interfacing with the skin,  
400 which is a naturally ionic medium. Hydrogels with high ionic conductivity can form  
401 low-impedance, conformal contacts with the stratum corneum, facilitating effective

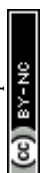


402 coupling with bioelectric signals such as ECG, EMG, or EEG. This enables stable, high-  
 403 fidelity acquisition of weak biopotentials with reduced signal loss or distortion.



404  
 405 **Fig. 5 Conductivity.** (a) Schematic illustrating the fabrication procedure of AgNWs-  
 406 PVA hydrogel composites by combining freezing and salting-out treatments. (b)  
 407 Conductivity of the AgNWs-PVA hydrogel composites with varying durations of  
 408 salting-out treatment. (c) Comparison of conductivity and fracture strain of the Ag-PVA  
 409 hydrogel with other conductive hydrogels based on different conductive fillers.  
 410 Reproduced with permission [107]. Copyright 2024, Wiley-VCH. (d) Schematic of  
 411 PVA-LM hydrogel network. (e) Conductivity of PVA-LM hydrogels with different  
 412 aging times. (f) The resistance response of PVA-LM hydrogel under cyclic stretching  
 413 for 1000 cycles. Reproduced with permission [108]. Copyright 2024, Wiley-VCH.

414 Conversely, electronic conductivity is vital for rapid and efficient transmission of the  
 415 collected signals to external readout devices. Materials such as PEDOT:PSS, CNTs, or  
 416 MXene can form continuous electron pathways that minimize resistance across the  
 417 electrode structure. In hybrid conductive hydrogels, the synergy between these two



418 conduction mechanisms enables high SNR, reduced motion artifacts, and stable  
419 performance under varying environmental and mechanical conditions. By combining  
420 the skin-compatible interface of ionic systems with the robust signal transfer capability  
421 of electronic systems, hybrid hydrogels offer a balanced and integrated solution for  
422 long-term, reliable epidermal bioelectronic applications.

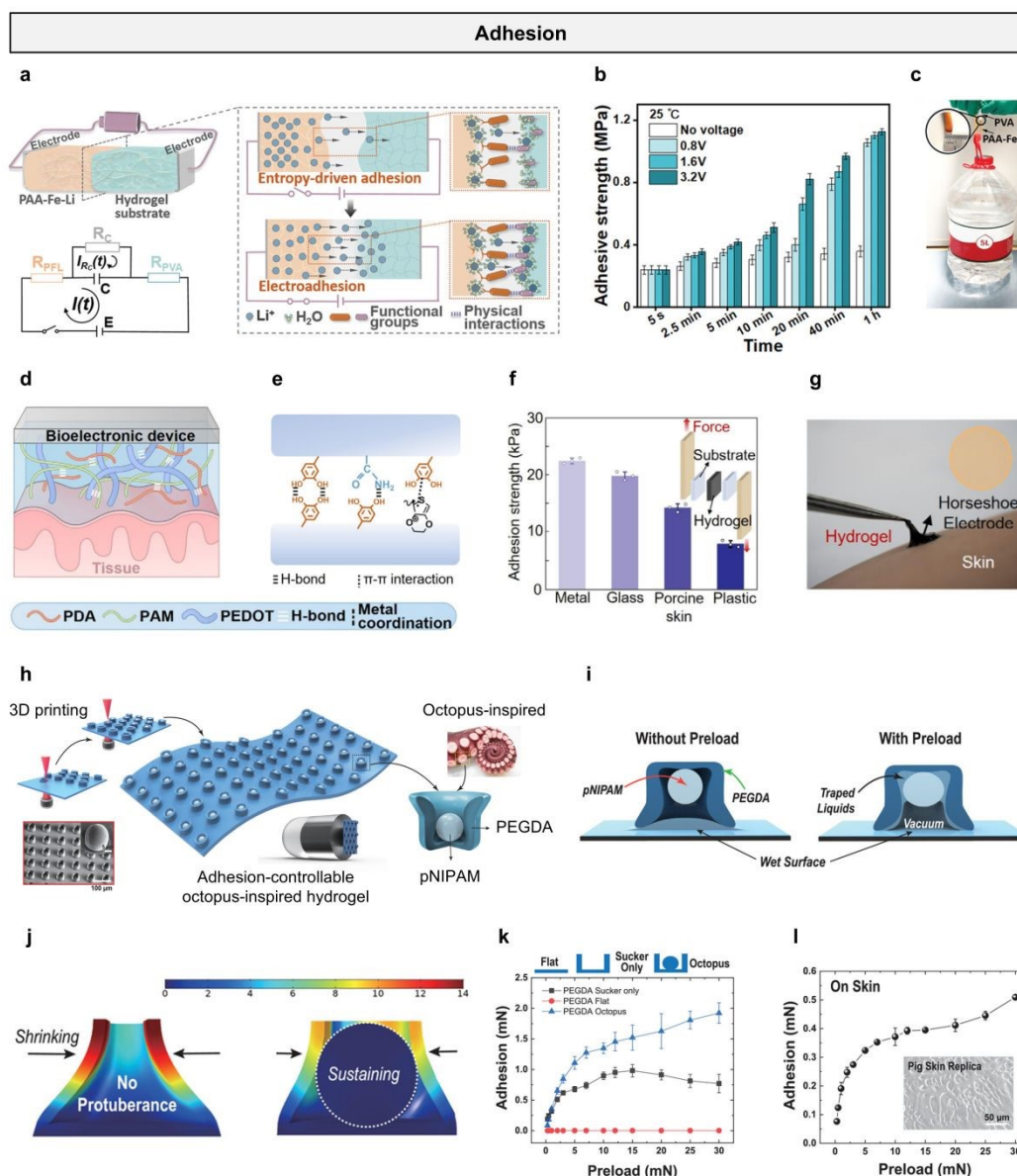
### 423 3.2 Adhesion

424 Superior adhesive properties enable hydrogel-based epidermal electrodes to effectively  
425 adhere to the skin, minimizing skin-contact impedance and enhancing the quality and  
426 stability of monitored signals<sup>109</sup>. To enhance the adhesive properties of conductive  
427 hydrogel-based epidermal electrodes, there are three typical mechanisms to enhance the  
428 adhesiveness of conductive hydrogel epidermal electrodes: physical adhesion, chemical  
429 adhesion, and biomimetic strategies<sup>110</sup>. In physical adhesion, external stimuli, including  
430 pH variations<sup>111</sup>, temperature fluctuations<sup>112</sup>, ultraviolet light<sup>113</sup>, magnetic fields<sup>114</sup>, and  
431 electric fields<sup>115</sup>, can be utilized to modulate the adhesive properties of hydrogels. A  
432 typical example is that Liu et al.<sup>116</sup> proposed an electro-adhesion strategy with  
433 electrically programmable strength for universal and super-strong hydrogel bonding.  
434 The hydrogel is composed of PAA-Fe-Li. Owing to the robust hydration capacity of  
435 Li<sup>+</sup> ions, they significantly modulate polymer chain interactions within the hydrogel,  
436 thereby enhancing its interfacial bonding through surface diffusion and accumulation  
437 (Fig. 6a). Driven solely by entropy related to the concentration gradient of the involved  
438 ions, PAA-Fe-Li exhibits effective adhesion to PVA hydrogels. After 5 seconds of  
439 contact, the adhesion strength and adhesion energy reach 0.24 MPa and 660 J/m<sup>2</sup>,  
440 respectively. Subsequently, under a positive DC voltage, the adhesion efficiency of  
441 PAA-Fe-Li to PVA at ambient temperature significantly increased by  $\approx 24$  times (Fig.  
442 6b). The peak adhesion strength and adhesion energy of PAA-Fe-Li with PVA  
443 substrates can reach 1.2 MPa and 3750 J/m<sup>2</sup>, respectively. Adhered PAA-Fe-Li and  
444 PVA samples with a cross-sectional diameter of 6 mm can withstand at least 5 kg of



445 weight (Fig. 6c).

446 In chemical adhesion, the adhesive effect is mainly caused by chemical bonding and/or  
 447 non-covalent interactions between reactive groups in the hydrogel and on the skin  
 448 surface<sup>110, 117</sup>. Covalent bonds play a predominant role in hydrogel adhesion due to their  
 449 higher bond energy relative to other interactions<sup>118</sup>. Non-covalent interactions,  
 450 including hydrogen and ionic bonds, are extensively employed in the fabrication of



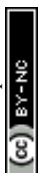
451

452 **Fig. 6 Adhesion.** (a) Mechanisms for strong interfacial bonding between the PAA-Fe-  
 453 Li hydrogel and hydrogel substrate and schematic illustration of the proposed circuit  
 454 model for electro-adhesion. (b) Adhesive strength of electro-adhesion between PAA-  
 455 Fe-Li and PVA hydrogels at 25 °C. (c) Strong adhesion (> 5 kg) demonstration between  
 456 PAA-Fe-Li and PVA. Reproduced with permission [116]. Copyright 2022, Wiley-VCH.



457 (d) Schematic illustration of a conventional bioelectronic device adhering directly to  
458 tissue. (e) Noncovalent interactions among dopamine methacrylate, PEDOT, PDA, and  
459 PAM chains. (f) Adhesion strength of hydrogel to different substrates by lap shear test.  
460 (g) Image of a hydrogel bioelectronic device for EMG and ECG monitoring.  
461 Reproduced with permission [87]. Copyright 2025, American Chemical Society. (h)  
462 Fabrication process of a polyethylene glycol diacrylate hydrogel. (i) Schematic  
463 illustration with finite element method simulation showing the adhesion mechanism of  
464 the sucker architecture with and without the inner protuberance structure. (j)  
465 Representative time-dependent profiles of adhesion results for the hydrogel patterns  
466 and flat glass for comparison. (k) Adhesion forces for different preloads (0.3–30 mN)  
467 in the samples of the inner pNIPAM and outer pNIPAM. (l) Adhesion results for  
468 different preloads (0.3 to 30 mN) in underwater conditions measured on the pig skin  
469 replica shown in inset. Reproduced with permission [119]. Copyright 2022, Wiley-  
470 VCH.

471 adhesive hydrogels to enhance interfacial adhesion<sup>120</sup>. Hydrogen bonds, distinguished  
472 for their adjustable strength, biocompatibility, and reversible bonding capabilities,  
473 represent a key intermolecular force. Generally, individual hydrogen bonds in  
474 hydrogels are weak, necessitating their synergistic combination with other interactions  
475 or the formation of multiple hydrogen bonds to enhance adhesion<sup>121</sup>. For example, Lao  
476 et al.<sup>87</sup> developed a hydrogel with inherent adhesion and conductivity by integrating  
477 PAM-polydopamine (PDA) into conductive PEDOT, exhibiting a tissue-mimetic  
478 modulus (Fig. 6d). The adhesion is formed through non-covalent interactions of  
479 hydrogen bonds and  $\pi$ - $\pi$  interactions with polydiacetylene and PAM chains (Fig. 6e).  
480 The shear strength of the hydrogel, adhered to various substrates including metal, glass,  
481 pig skin, and plastic, was measured at 22.4, 19.8, 14.2, and 7.9 kPa, respectively (Fig.  
482 6f). Due to its ultra-soft and strong adhesive properties, the conductive hydrogel  
483 epidermal electrode can form a tight and robust interface with human tissue, thereby  
484 reducing artifacts caused by body movement (Fig. 6g). In biomimetic structures, the  
485 adhesion mechanisms of various organisms (including tree frogs, mussels, octopuses,  
486 and geckos) have attracted numerous researchers and inspired the development of  
487 biomimetic hydrogels<sup>122, 123</sup>. For instance, the eight arms of an octopus are equipped  
488 with numerous suckers, each generating negative pressure via muscle control to  
489 produce robust adhesion<sup>124</sup>. This mechanism, independent of chemical adhesives,



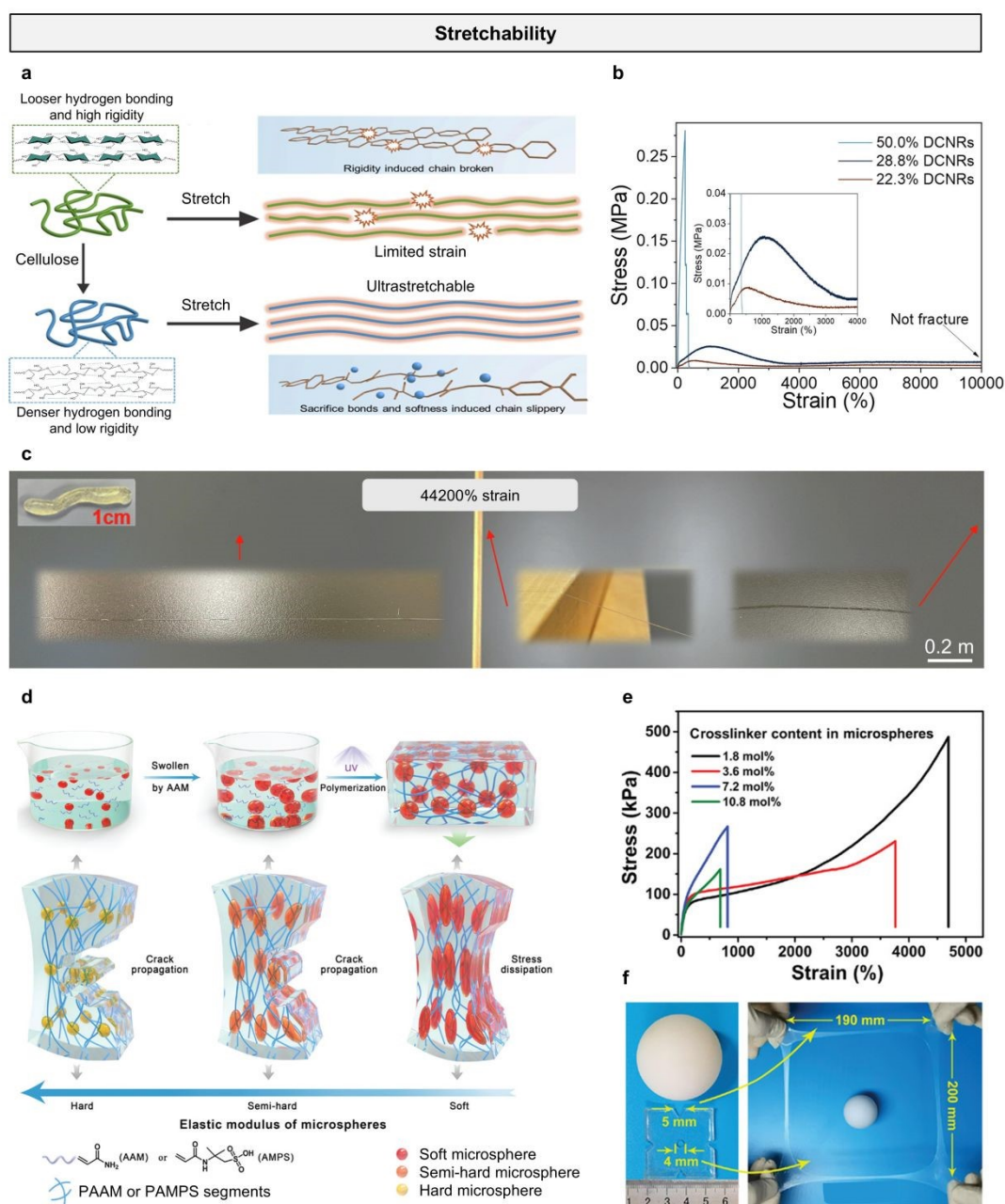
490 enables secure attachment to wet or irregular surfaces, such as marine rocks or prey.  
491 These attributes inspire the development of high-performance, reusable biomimetic  
492 adhesive materials tailored for complex environments. Inspired by the octopus's orifice,  
493 Lee et al.<sup>119</sup> printed polyethylene glycol diacrylate (pNIPAM) hydrogel to form an outer  
494 wall, completing an internal dome-shaped structure mimicking octopus protrusions,  
495 which enhanced dry and wet adhesion (Fig. 6h). The pNIPAM achieves robust wet  
496 adhesion under external preload by inducing cohesive forces among liquid molecules  
497 at interacting wet surfaces (Fig. 6i and 6j). Due to the enhancement of suction, the  
498 sucker with an internal dome-like protrusion structure can enhance adhesion in wet  
499 environments (Fig. 6k). Adhesion was evaluated under preloads ranging from 0.5 to 30  
500 mN on a skin-mimicking surface. Owing to the roughness of pig skin, adhesion on pig  
501 skin was approximately three times lower or more than that on a smooth glass surface  
502 (Fig. 6l).

### 503 3.3 Stretchability

504 Beyond essential conductivity and adhesion, superior tensile performance is a critical  
505 attribute that positions hydrogels as ideal materials for stretchable epidermal electrodes.  
506 This capability allows hydrogel-based electrodes to effectively accommodate body  
507 deformations while sustaining conformal contact, ensuring reliable signal  
508 transmission<sup>27</sup>. Typical strategies for enhancing the mechanical properties of hydrogel  
509 epidermal electrodes include constructing multiple crosslinked network structures,  
510 adding nanocomposites, introducing supramolecular interactions, etc<sup>102, 125</sup>. For  
511 example, Zhang et al.<sup>126</sup> developed an all-cellulose hydrogel with exceptional  
512 stretchability by introducing supramolecular structures through the ring-opening  
513 reaction of cellulose's anhydroglucose units via dehydration (Fig. 7a). The hydrogel's  
514 tensile properties were enhanced by modifying the cellulose structure and tuning  
515 interchain interactions. To increase chain flexibility, periodate oxidation was employed  
516 to selectively cleave the C2–C3 bond, converting secondary hydroxyl groups into

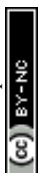


517 aldehyde groups and thereby opening the anhydroglucose ring structure. The resulting  
 518 hydrogel exhibited a record-breaking tensile of 42200% strain. The mechanical  
 519 properties of the hydrogel were significantly influenced by the content of diol cellulose  
 520 nanorods (DCNRs). As the DCNR content increased from 23.3 to 28.8%, the tensile  
 521 stress rose progressively from 7 to 25 kPa. When the DCNR content ranged from 23.3  
 522 to 28.8%, the strain of the hydrogels exceeded 10000% strain. (Fig. 7b). To further  
 523 validate the hydrogel's stretchability, a 1 cm hydrogel was stretched to 4.42 m,



524

525 **Fig. 7 Stretchability.** (a) Schematic illustration of the cleavage of rigid anhydroglucose  
 526 unit rings enhances hydrogel chain flexibility and facilitates the reformation of

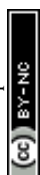




527 hydrogen bonds during tensile deformation. (b) Stress-strain curves under different  
528 DCNRs contents. (c) Photos of DCNRs hydrogel before and after stretching.  
529 Reproduced with permission [126]. Copyright 2024, Wiley-VCH. (d) Schematic  
530 illustration of the preparation process and mechanism of super-stretchable hydrogel. (e)  
531 Tensile curves of hydrogels under different cross-linker concentrations. (f) Tear  
532 resistance of 5 mm long hydrogel under pre-cut equilateral triangle notch. Reproduced  
533 with permission [127]. Copyright 2022, Wiley-VCH.

534 corresponding to a strain of 42200% (Fig. 7c). Ji et al.<sup>128</sup> introduced an IL imidazolium  
535 salt with a urea backbone (UL) and incorporated sulfobetaine methacrylate (SBMA)  
536 and acrylamide (AM) into the hydrogel system (ULAS) through simple one-pot  
537 copolymerization. Supramolecular interactions within the IL strengthen the non-  
538 covalent bond network of hydrogel-based epidermal electrodes. As the IL concentration  
539 increases, the hydrogel exhibits markedly enhanced stress, achieving an elongation at  
540 break of 1075% strain and a fracture stress of 343 kPa. Constructing physically  
541 crosslinked, entangled, and micelle-crosslinked networks has been demonstrated as an  
542 effective way to enhance the mechanical properties of hydrogels. Li et al.<sup>127</sup>. prepared a  
543 highly stretchable hydrogel with an interpenetrating entangled network by using PAM  
544 as the monomer and poly(1-acrylamido-2-methylpropanesulfonic acid) (PAMPS) as  
545 the physical crosslinking network, synthesized via UV-initiated free radical  
546 polymerization (Fig. 7d). The mechanical properties of hydrogels can be tuned by  
547 varying the crosslinker concentration. The fracture strain of hydrogels decreases rapidly  
548 with increasing crosslinking degree, reaching 4700% strain at a crosslinker content of  
549 1.8 mol% (Fig. 7e). Furthermore, the hydrogel demonstrates outstanding tear resistance.  
550 Hydrogels with a 5 mm pre-cut notch extended to 190 mm and 200 mm under tensile  
551 stress without crack propagation. The area of a central circular pre-cut notch expanded  
552 approximately 2700-fold during cyclic biaxial stretching (Fig. 7f). Li et al.<sup>54</sup> developed  
553 a hydrogel with a multiply crosslinked network by incorporating gelatin and SA into  
554 PAM. With the addition of SA, a more complex network structure is formed between  
555 PAM/gelatin and SA through hydrogen bonds and electrostatic interactions between  
556 molecular chains. As the SA content rises from 0 to 0.8 wt%, the hydrogel's tensile  
557 stress increases from 61.3 to 229.3 kPa, with the elongation at break improving from

View Article Online  
DOI: 10.1039/D5TC01896J



558 428.4 to 706.4% strain.

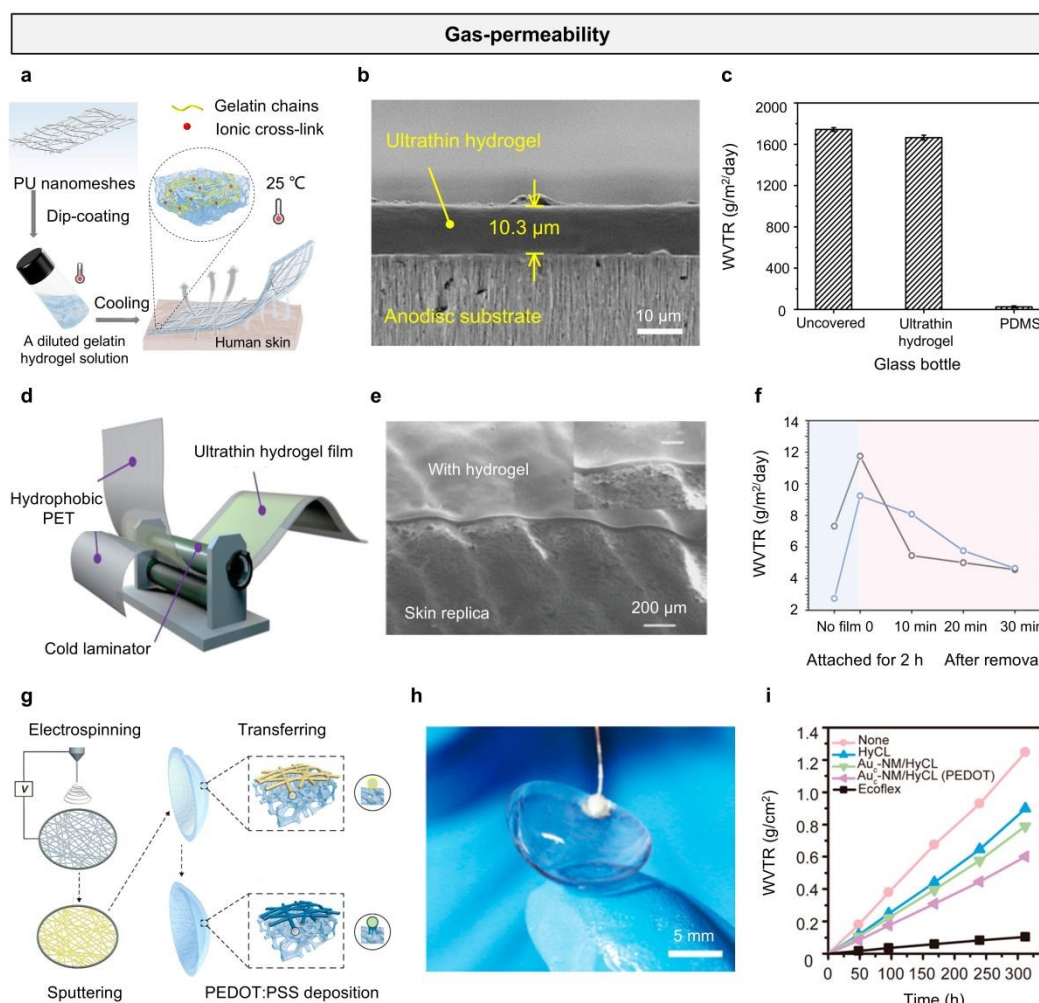
### 559 **3.4 Gas-permeability**

560 Water vapor and sweat accumulation at the skin-electrode interface can lead to skin  
561 irritation and epidermal electrode failure during prolonged monitoring<sup>129</sup>. Employing  
562 gas-permeable conductive hydrogel-based epidermal electrodes has proven an effective  
563 solution to this challenge<sup>130</sup>. Common strategies for enhancing the gas-permeability of  
564 conductive hydrogel-based epidermal electrodes include fabricating ultrathin and  
565 porous structures<sup>129, 131</sup>. A typical example is that Zhang et al.<sup>49</sup> introduced an ultrathin  
566 polyurethane (PU) nanomesh-reinforced gas-permeable hydrogel. The hydrogel was  
567 fabricated by immersing the PU nanomeshes in a temperature-sensitive gelatin-based  
568 hydrogel solution (Fig. 8a). The resulting ultrathin hydrogel has a thickness of ~10.3  
569  $\mu\text{m}$  (Fig. 8b), with excellent mechanical strength (up to 696% strain) and high skin  
570 adhesion (area adhesion energy of  $176.8 \mu\text{J}/\text{cm}^2$ ). Owing to its ultrathin geometry and  
571 porous structure, the hydrogel demonstrates a water vapor transmission rate (WVTR)  
572 of  $1669.3 \pm 23.5 \text{ g}/\text{m}^2/\text{day}$ , closely comparable to that of an open bottle ( $1742.8 \pm 18.3$   
573  $\text{g}/\text{m}^2/\text{day}$ ) (Fig. 8c). The resultant ultrathin hydrogel-based epidermal electrode enables  
574 long-term, continuous, high-precision electrophysiological monitoring for up to 8 days  
575 under everyday conditions.

576 Cheng et al.<sup>132</sup> developed a cold lamination-based approach to fabricate breathable  
577 hydrogel films with precisely controlled thickness and scalability. A mixed solution of  
578 PAM and SA is cast between two polyethylene terephthalate (PET) support films and  
579 then rapidly passed through the gap between two rollers. The prepared PET-wrapped  
580 hydrogel precursor film is cured under ultraviolet light to complete in-situ gelation (Fig.  
581 8d). The prepared hydrogel film thickness can be controlled to a minimum of  $7 \mu\text{m}$ .  
582 The ultrathin hydrogel film has good skin conformability, and cross-sectional SEM  
583 images show close contact between a fingerprint replica and a  $10 \mu\text{m}$  thick hydrogel  
584 film (Fig. 8e). Due to its ultrathin characteristics, the hydrogel film has good

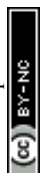


585 breathability, measured by transepidermal water loss (TEWL). A 50  $\mu\text{m}$  thick hydrogel  
 586 film and a 3  $\mu\text{m}$  thick impermeable parylene film were attached to the skin, respectively.  
 587 After applying the ultrathin acrylic film for 2 hours, the initial skin hydration level  
 588 increased from approximately 25 to 45%. Accompanying this, the TEWL significantly  
 589 increased from  $\sim 7$  to 12  $\text{g}/\text{m}^2/\text{day}$ . After removing the acrylic film, the skin moisture  
 590 level dropped to  $\sim 28\%$  within 30 minutes, and the TEWL also decreased (Fig. 8f).



591

592 **Fig. 8 Gas-permeability.** (a) Schematic illustration of the design concept of PU  
 593 nanomesh-reinforced hydrogels. (b) Cross-sectional SEM image of the ultrathin  
 594 hydrogel attached on an anodisc substrate. (c) Comparison of WVTR for an uncovered  
 595 bottle, a bottle covered with 1000- $\mu\text{m}$ -thick PDMS film, and a bottle covered with  $\sim 10$ -  
 596  $\mu\text{m}$ -thick ultrathin hydrogel, respectively. Reproduced with permission [49]. Copyright  
 597 2024, American Association for the Advancement of Science. (d) Schematic of the  
 598 cold-lamination method to produce large-area ultrathin hydrogel films. (e) SEM images  
 599 of a 10  $\mu\text{m}$  thick hydrogel film attached to the fingerprint replica. (f) TEWL and the  
 600 skin hydration level test by attaching a 3  $\mu\text{m}$  thick parylene film on the forearm of the



601 volunteer. (g) Schematic illustration of the gas-permeable, irritation-free, transparent  
602 hydrogel film. Reproduced with permission [132]. Copyright 2022, Wiley-VCH. (h)  
603 Picture of a contact lens-based eye interfacing device based on the hydrogel film. (i)  
604 WVTR of open bottle (none), pure hydrogel ocular contact lens (HyCL), HyCL with  
605 gold-coated nanofiber mesh (Auc-NM/HyCL), Auc-NM/HyCL with deposition of  
606 PEDOT:PSS, and Ecoflex film as a function of elapsed time. Reproduced with  
607 permission [133]. Copyright 2019, American Chemical Society.

608 Wei et al.<sup>133</sup> reported a breathable, non-irritative, and transparent hydrogel film. The  
609 gas-permeable film was fabricated using a metal-coated nanofiber network (metal<sub>c</sub>-NM)  
610 as the electronic conductor and a commercial hydrogel contact lens as the substrate,  
611 with in situ electrochemical deposition of PEDOT:PSS employing the metal<sub>c</sub>-NM as  
612 the electrode (Fig. 8g). The resultant hydrogel film exhibits an optical transparency of  
613 90% (Fig. 8h). Owing to the highly porous structure of the metal<sub>c</sub>-NM film, the  
614 underlying hydrogel substrate retains its breathability, enabling the hydrogel film to  
615 demonstrate excellent breathability with a WVTR of approximately 69.2 mg/cm<sup>2</sup>/day,  
616 significantly exceeding that of an impermeable Ecoflex film at 7.98 mg/cm<sup>2</sup>/day (Fig.  
617 8i).

#### 618 **4. Applications of Conductive Hydrogel-based Epidermal Electrodes in** 619 **Electrophysiological Monitoring**

620 Conductive hydrogel-based epidermal electrodes, due to their good conductivity,  
621 outstanding skin adhesion and compliance, excellent stretchability, and superior  
622 breathability, have shown great potential in the field of electrophysiological signal  
623 monitoring. In this section, we will summarize the representative progress of  
624 conductive hydrogel-based epidermal electrodes in ECG, EMG, EEG, and EOG  
625 monitoring.

##### 626 **4.1 Electrocardiogram monitoring**

627 ECG signals play a pivotal role in the medical field, being extensively utilized for



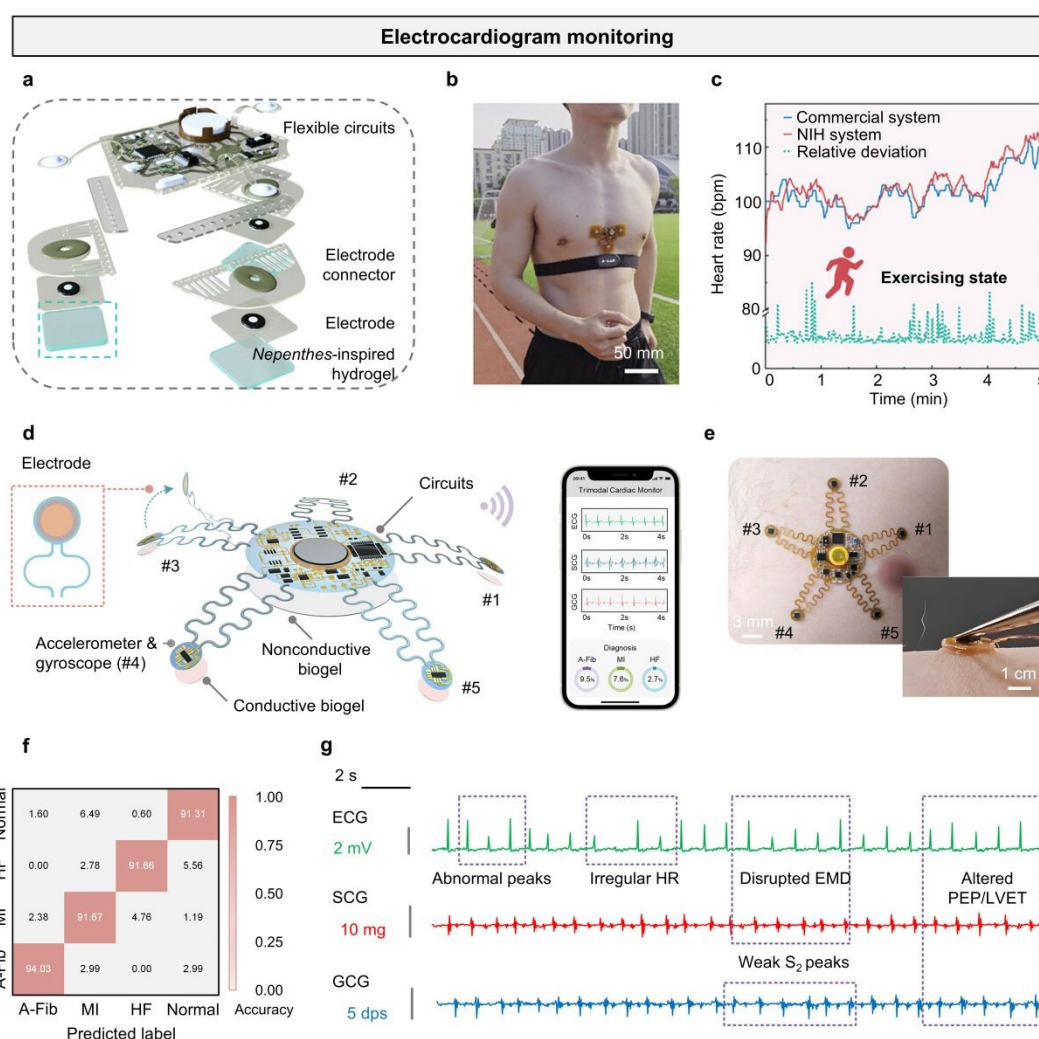
628 diagnosing cardiovascular diseases<sup>134-137</sup>, and assessing cardiac health<sup>138,140</sup>.  
629 Conductive hydrogel-based epidermal electrodes possess distinctive properties,  
630 including high conductivity, excellent stretchability, and strong interfacial adhesion<sup>141</sup>,  
631 <sup>142</sup>. These attributes enable them to achieve superior SNR and sensitivity compared to  
632 traditional rigid electrodes, thereby enhancing the accuracy and reliability of  
633 monitoring and providing more precise data to support clinical diagnostics and  
634 treatment.

635 A typical example is that Yang et al.<sup>143</sup> developed a wireless Nepenthes-inspired  
636 hydrogel (NIH) hybrid system. The hybrid system consists of a skin electrode  
637 assembled from a flexible circuit module, an electrode connector with a hollow  
638 structure, a stretchable silicone joint, and three Nepenthes-inspired hydrogel interface  
639 layers (Fig. 9a). The DN hydrogel based on PVA/PAA enhances its adhesion to the skin  
640 (3.9 kPa). To evaluate the practicality of the NIH hydrogel system during motion, the  
641 system was laminated on the skin above the subject's heart to collect ECG signals (Fig.  
642 9b). To evaluate the stability of the NIH system, heart rate curves were recorded using  
643 the system and a commercial device (i.e., Polar H10 heart rate strap) under motion  
644 conditions, respectively. The results demonstrate that data from both systems reveal  
645 nearly identical heart rate variation trends, with a relative deviation of less than 2.6%  
646 over 5 minutes, validating the accuracy of the NIH system (Fig. 9c).

647 Inspired by the pentaradial symmetry of starfish, Chen et al.<sup>144</sup> introduced a starfish-  
648 like wearable hydrogel-based bioelectronic system for high-fidelity ECG monitoring.  
649 The skin interface layer consists of conductive hydrogels for five sensing pads and non-  
650 conductive hydrogels for the central hub, while the serpentine arms remain independent.  
651 The device is constructed on a 25  $\mu\text{m}$ -thick polyimide (PI) substrate, utilizing copper  
652 traces as conductive pathways. Its pentaradial design incorporates five serpentine arms,  
653 each equipped with an independent sensing element at its tip, all linked to a central  
654 electronic hub for data processing and wireless transmission. Signals are processed by  
655 a 32-bit microcontroller and transmitted wirelessly, with analyzed data presented



656 intuitively on a mobile device (Fig. 9d). By employing a conductive adhesive hydrogel  
 657 as the electrode-skin interface and a mechanically decoupled starfish-inspired device  
 658 design (Fig. 9e), this device enables high-fidelity ECG recordings across diverse  
 659 motion states, sustaining an SNR of approximately 35 dB even during running. The  
 660 system enables real-time, high-precision diagnosis of cardiac conditions by integrating  
 661 ECG, seismocardiogram, and gyrocardiogram signals with a deep learning model,  
 662 achieving classification accuracies of 91.31% for normal conditions, 94.03% for atrial



663  
 664 **Fig. 9 Electrocardiogram monitoring.** (a) Exploded 3D model of the NIH hybrid  
 665 system. (b, c) Heart rate and relative deviation curves measured by the NIH system and  
 666 commercial system under the subject's exercising states. Reproduced with permission  
 667 [143]. Copyright 2024, Wiley-VCH. (d) Schematic illustration of the starfish-like  
 668 device for trimodal cardiac monitoring during motion. (e) Optical image showing the  
 669 device applied to the chest skin, with the five strategically positioned sensing pads, and  
 670 optical image, showing robust adhesion of the sensing pad to human skin, facilitated by  
 671 the conductive hydrogels. The image features a tweezer used to stretch the sensing pad



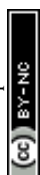
672 from the skin. (f) Confusion matrix, demonstrating the classification accuracy for  
673 predicting each type of heart disease and normal signals in the test set. During use, the  
674 starfish-like device can display the real-time classification probabilities on smart  
675 devices. (g) Cardiac electrical and mechanical signals collected by the starfish-like  
676 wearable device from a HF patient during walking; dps, degrees per second.  
677 Reproduced with permission [144]. Copyright 2025, American Association for the  
678 Advancement of Science.

679 fibrillation, 91.67% for myocardial infarction, and 91.66% for heart failure. Fig. 9f  
680 shows the cardiac mechanical and electrical biosignals captured by a hydrogel-based  
681 device during walking in a patient clinically diagnosed with heart failure. The signals  
682 show reduced Q and T peaks, irregular heart rate, interrupted electromechanical delay,  
683 and altered pre-ejection period/left ventricular ejection time parameters, indicating  
684 electrophysiological disturbances. Additionally, the patient's cardiac mechanical  
685 activity is significantly impaired, with a contraction amplitude nearly 60% lower than  
686 that of healthy individuals (Fig. 9g). These results demonstrate the ability of hydrogel-  
687 based epidermal electrodes to achieve high-fidelity recording of cardiac signals.

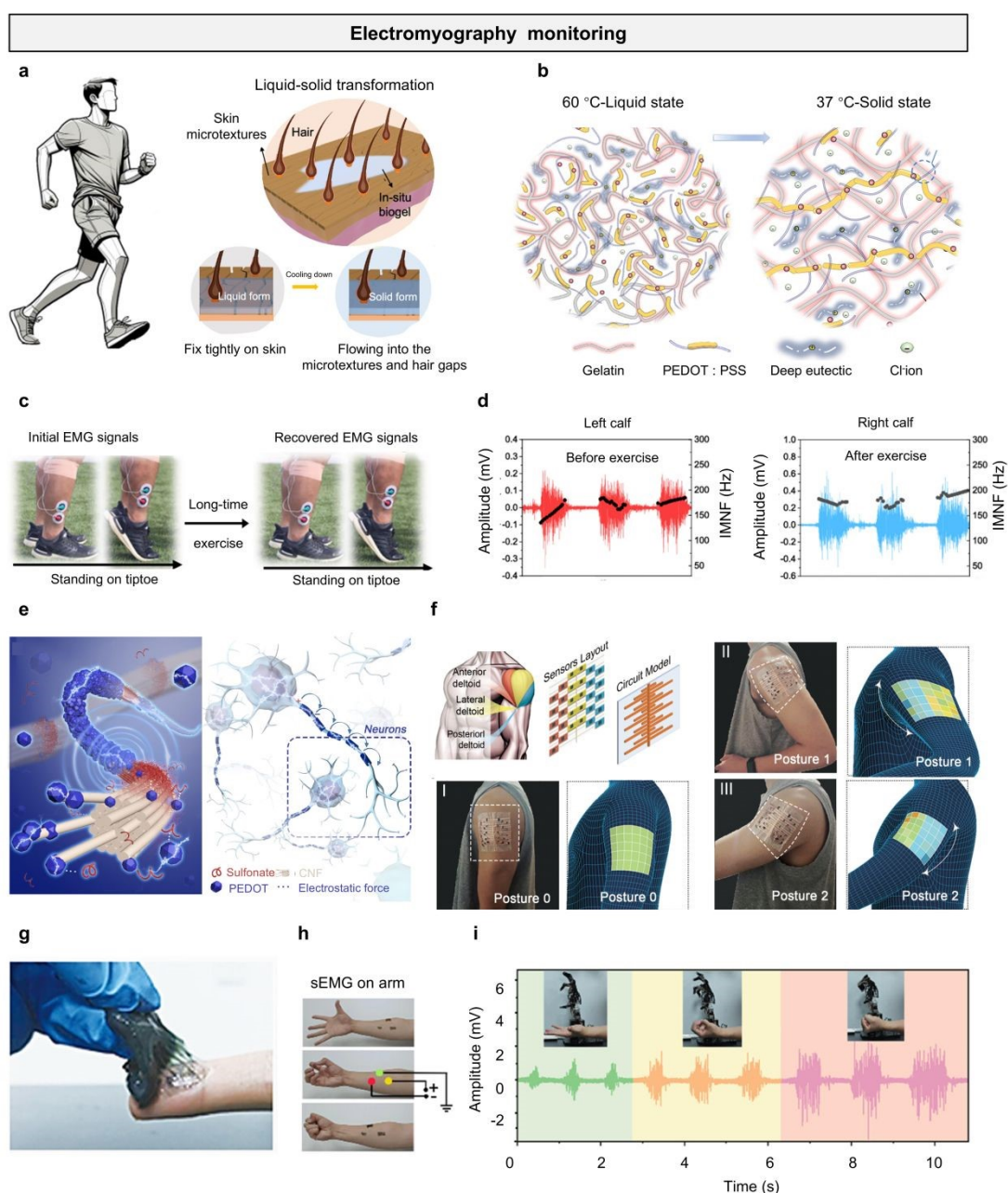
## 688 4.2 Electromyography monitoring

689 EMG is a technique for recording electrophysiological activity associated with muscle  
690 contraction and relaxation<sup>145</sup>. As EMG signals directly reflect neuromuscular activity,  
691 they are extensively utilized in human motion monitoring<sup>146-148</sup>, controlling human-  
692 machine interfaces<sup>149-151</sup>, and diagnosing neuromuscular disorders<sup>45, 152, 153</sup>. However,  
693 the impedance between the electrode and skin affects the quality of EMG signals in  
694 practical applications, so researchers have increasingly focused on enhancing the  
695 conductivity and skin adhesion of hydrogel-based epidermal electrodes to achieve low  
696 interface impedance<sup>142, 154-157</sup>. For instance, Tian et al.<sup>158</sup> leveraged the liquid-to-solid  
697 transition concept to develop an in-situ hydrogel-based epidermal electrode for  
698 monitoring post-fatigue muscle recovery (Fig. 10a). To develop a hydrogel with rapid  
699 in situ gelation, a formulation of gelatin, PEDOT:PSS, and a deep eutectic solvent (DES)  
700 was employed. At temperatures above 60 °C, gelatin exists as individual molecular

View Article Online  
DOI: 10.1039/D5TC01896J



701 chains. Upon cooling, the gelatin network solidifies via hydrogen bonding and physical  
 702 crosslinking, with PEDOT:PSS forming a conductive network within the gelatin matrix  
 703 (Fig. 10b). DES demonstrate superior thermal stability and ionic conductivity. The  
 704 hydroxyl groups in DES engage with the polymer network via hydrogen bonding and  
 705 ionic interactions, improving solubility, stability, and network formation. The in situ-  
 706 formed hydrogel exhibits exceptional adhesion (591 kPa) and minimal skin contact  
 707 impedance (10.2 k $\Omega$ ). The prepared in-situ biogel epidermal electrode was used to



708 **Fig. 10 Electromyography monitoring.** (a) Liquid-to-solid transformation concept  
 709 and the application of in situ biogel. (b) Schematic diagram and optical images of the  
 710





711 in situ rapid gelation process of the biogel. (c) Procedure for recovery monitoring using  
712 in situ biogel. Comparison of initial EMG signals with those after fatigue. (d) Initial  
713 EMG signals and post-exercise signals for left and right calves. Reproduced with  
714 permission [158]. Copyright 2025, Nature Publishing Group. (e) Schematic illustration  
715 of the biomimetic segmentally conductive fiber hydrogel. (f) Sensor array layout and  
716 circuit model designed for monitoring muscle movements. (j) Photograph of the self-  
717 adhesive hydrogel after peeling. (h, i) EMG signals on the forearm at different grip  
718 force levels. Reproduced with permission [99]. Copyright 2024, American Chemical  
719 Society.

720 monitor muscle recovery after exercise-induced fatigue. EMG signals from the left and  
721 right calves were recorded when volunteers performed toe-raising exercises (Fig. 10c).  
722 After prolonged exercise (running for 45 minutes), the hydrogel epidermal electrode  
723 recorded EMG signals at different stages, with an SNR of up to 30 dB (Fig. 10d).  
724 Hydrogel-based epidermal electrodes were employed to monitor muscle signals in  
725 volunteers during extended sedentary periods, revealing a decline in average muscle  
726 frequency over time. After 24 hours, the mean muscle frequency started to rise,  
727 approaching pre-exercise levels by 48 hours, signifying full recovery from exercise-  
728 induced fatigue. To quantitatively assess muscle fatigue recovery, the recovery  
729 percentage was defined as the ratio of mean EMG frequencies before and after exercise-  
730 induced fatigue. This recovery metric enables precise evaluation of muscle condition,  
731 supporting exercise and recovery planning, as well as monitoring recovery from  
732 muscle-related disorders. Liu et al.<sup>99</sup> designed high-performance hydrogel-based  
733 epidermal electrodes by incorporating numerous interpenetrating core-sheath  
734 conductive nanofibers into a physically crosslinked polyelectrolyte network. The  
735 hydrogel is composed of cellulose nanofibers, PAA, and PEDOT:PSS (Fig. 10e). The  
736 hydrogel-based epidermal electrode was fabricated as a  $10 \times 10 \text{ cm}^2$  multi-pixel skin  
737 array, showcasing its capability to capture human motion across various postures (Fig.  
738 10f). As an interface for human-machine interaction, the hydrogel epidermal electrode  
739 exhibits good interfacial adhesion (adhesion energy of 28 kPa on pig skin) and a low  
740 electrochemical impedance of  $42 \Omega$ . Fig. 10g shows that after peeling from the skin, a  
741 typical “fibrillation” phenomenon occurs, confirming effective adhesion between the

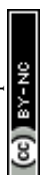
View Article Online  
DOI: 10.1039/D5TC01896J



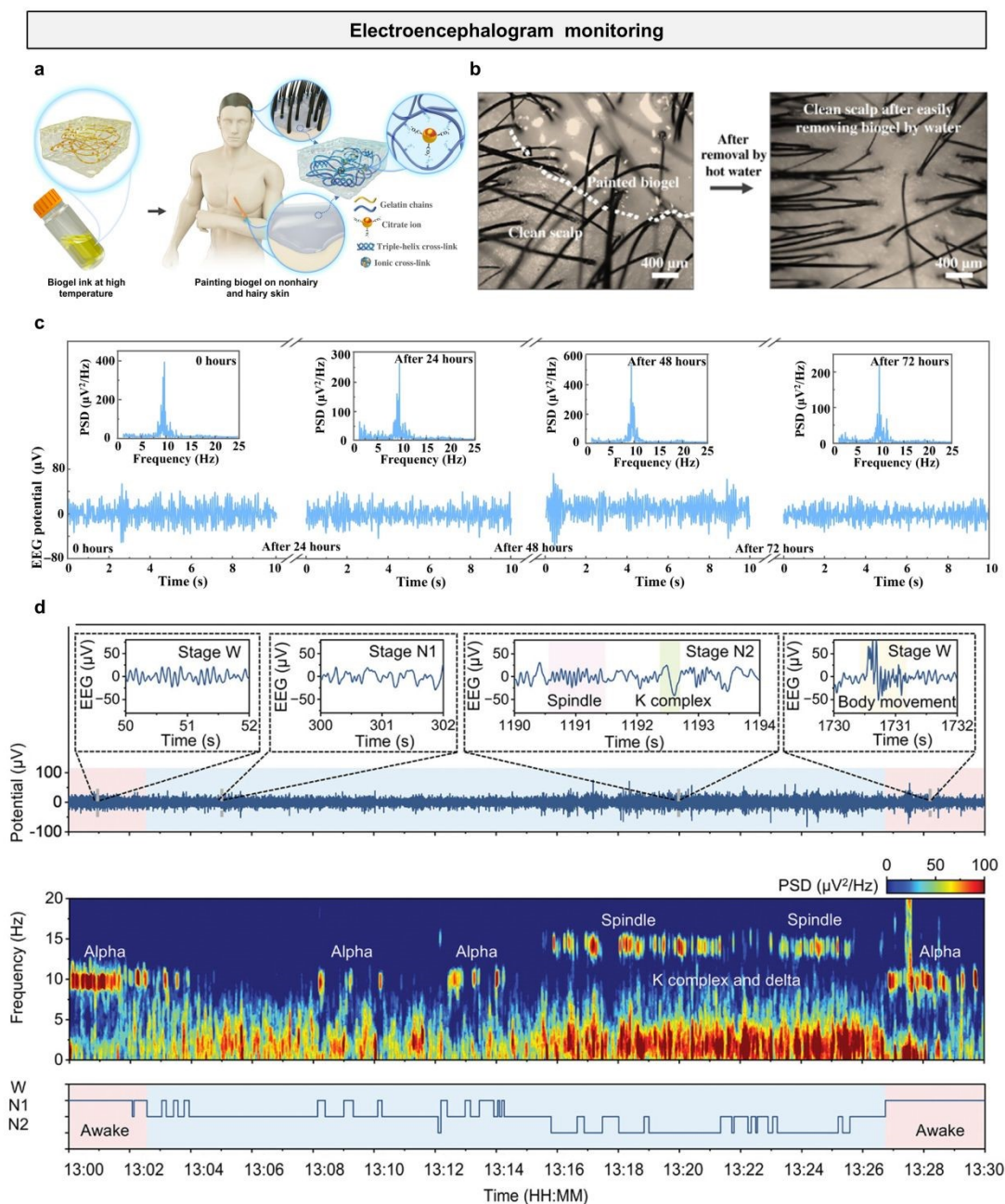
742 hydrogel epidermal electrode and the skin (Fig. 10h). To evaluate the human-machine  
743 interaction capability of the hydrogel epidermal electrode, the electrode was used to test  
744 EMG signals on the forearm under different grip strength levels, and the recorded arm  
745 EMG signals could be customized to precisely control a prosthetic limb, thereby  
746 achieving various robotic gestures with adjustable grasping angles and force levels (Fig.  
747 10i).

### 748 4.3 Electroencephalogram monitoring

749 EEG is an electrophysiological monitoring method for recording brain electrical  
750 activity.<sup>159</sup> It mainly originates from postsynaptic potentials and has significant  
751 application potential in sleep monitoring<sup>160-162</sup>, emotion recognition<sup>163-165</sup>, and brain-  
752 computer interfaces<sup>166-168</sup>. The presence of scalp hair and the head's intricate, curved  
753 contours pose significant challenges in achieving stable and effective contact between  
754 epidermal electrodes and the scalp for prolonged EEG recordings<sup>169</sup>. To overcome this  
755 challenge, Wang et al.<sup>170</sup> developed a conductive gel-based epidermal electrode for skin  
756 application, featuring a temperature-responsive reversible liquid-to-gel transition. This  
757 phase transition endows the hydrogel with unique skin coating and in-situ gelation  
758 properties (Fig. 11a). The fluidity of the conductive hydrogel enables good compliance  
759 and conformal contact with hairy scalps without hair interference, surpassing  
760 prefabricated gels, which facilitates high-quality EEG recording through hairy scalps  
761 (Fig. 11b). The conductive hydrogel-based epidermal electrode was utilized to capture  
762 EEG signals during open-eye and closed-eye conditions, revealing distinct differences  
763 between the signals in these paradigms. Due to its relatively long-term electrical  
764 stability, excellent mechanical interaction ( $73.4 \pm 2.2$  kPa), and stable contact with the  
765 scalp ( $6.95 \pm 0.97$  k $\Omega$ ), the conductive hydrogel epidermal electrode recorded  $\alpha$  signals  
766 with no significant differences across different wearing durations (0, 24, 48, and 72  
767 hours), with high quality and a peak frequency of 10 Hz (Fig. 11c). This indicates that  
768 the applicable conductive hydrogel epidermal electrode has promising capabilities for



769 long-term high-fidelity EEG recording. To enable continuous high-fidelity EEG signal  
 770 detection, paintable hydrogel-based epidermal electrodes require a streamlined and  
 771 rapid gelation process to minimize adhesion-related damage from slow gelation and  
 772 reduce subject discomfort. Li et al.<sup>171</sup> developed a paintable, fast-gelling, and highly  
 773 adhesive hydrogel-based epidermal electrode via a one-pot synthesis. Comprising  
 774 gelatin, gallic acid, sodium citrate, LiCl, glycerol, and Tris-HCl buffer (Gel-GGLiCit),



775  
 776 **Fig. 11 Electroencephalogram monitoring.** (a) Schematic illustration showing the  
 777 concept of on-skin paintable biogel for hairy scalp for EEG recording. (b) Optical  
 778 images of biogel painted on the hairy scalp and clean scalp after removing biogel by



779 water. (c) EEG alpha rhythms recorded by the painted biogel electrode after continuous  
780 wearing for 0, 24, 48, and 72 hours. Reproduced with permission [170]. Copyright 2022,  
781 American Association for the Advancement of Science. (d) Continuous wireless  
782 monitoring of EEG signals using paintable Gel-GGLiCit hydrogels and the multitaper  
783 spectrogram of the EEG signals (top) and visually scored hypnogram (bottom).  
784 Reproduced with permission [171]. Copyright 2024, Wiley-VCH.

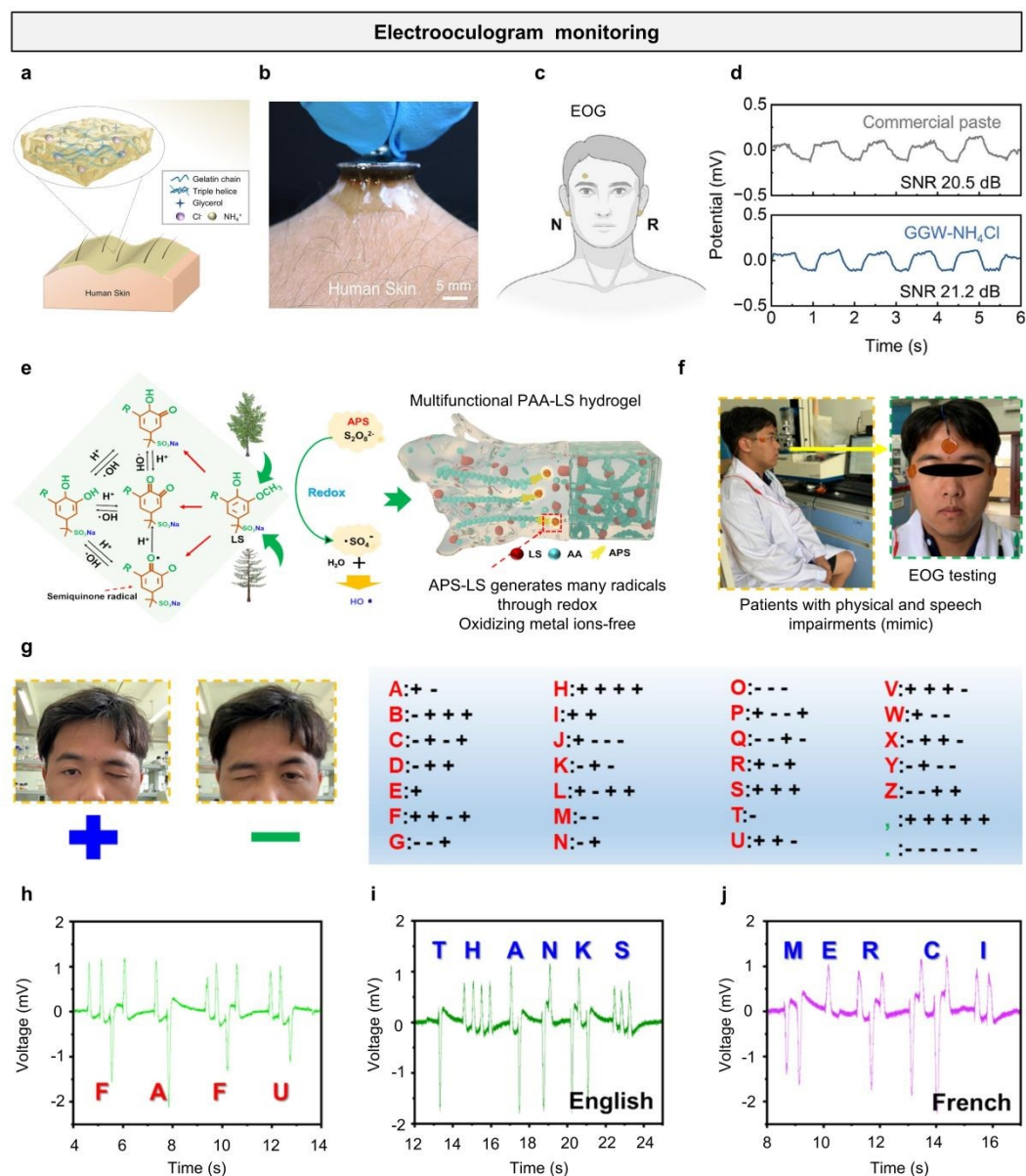
785 the hydrogel possesses reversible thermal phase transition properties, facilitating skin  
786 compatibility and rapid in situ gelation within 15 seconds. Furthermore, the paintable  
787 hydrogel-based epidermal electrode can form a conformal interface with hairy scalps  
788 ( $3.36 \text{ mJ/cm}^2$ ) in its fluid state prior to gelation, allowing it to penetrate dense hair  
789 effectively. These properties substantially lower scalp contact impedance, with the  
790 electrode achieving a reduced skin contact impedance of  $45.64 \text{ k}\Omega$  compared to  $62.70$   
791  $\text{k}\Omega$  for commercial pastes. To assess the potential of the paintable hydrogel-based  
792 epidermal electrode for sleep stage monitoring and sleep disorder analysis, it was  
793 employed to capture EEG signals from subjects during brief daytime naps. In addition  
794 to the awake state, the subject's 30-minute sleep primarily involved non-rapid eye  
795 movement (NREM) sleep, stages N1 and N2. Stage N1 marks the initial phase of sleep,  
796 defined by the transition from wakefulness to sleep, where individuals experience light  
797 sleep and are easily roused. Following N1, stage N2 emerges as a deeper sleep phase,  
798 characterized by a reduced heart rate and the occurrence of sleep spindles (Fig. 11d).  
799 During the awake stage (W), elevated power in the alpha band (8–12 Hz) is evident in  
800 EEG signals, most pronounced during eye closure. As wakefulness transitions to stage  
801 N1, alpha band power progressively diminishes and eventually disappears. These  
802 findings demonstrate that high-fidelity raw EEG data, acquired with paintable  
803 hydrogel-based epidermal electrodes, enable clear visualization of critical EEG features  
804 throughout sleep.

#### 805 4.4 Electrooculography monitoring

806 EOG is a technique that measures eye movement and position by recording electrical  
807 potentials around the eyes, widely used for diagnosing ophthalmic and neurological



808 disorders<sup>172, 173</sup>, supporting human-computer interaction<sup>174, 175</sup>, studying cognitive  
 809 processes<sup>176, 177</sup>, and assessing fatigue and alertness<sup>178, 179</sup>. Zheng et al.<sup>180</sup> developed a  
 810 thermoresponsive gelatin-based hydrogel (GGW) via a one-pot synthesis, incorporating  
 811 glycerol, ammonium chloride (NH<sub>4</sub>Cl), and water (Fig. 12a). The in situ-formed  
 812 hydrogel electrode demonstrates robust adhesion at the hydrogel-skin interface (0.9  
 813 N/cm), enabling conformal skin contact and high-fidelity signal acquisition (Fig. 12b).



814  
 815 **Fig. 12 Electrooculography monitoring.** (a) Schematic view depicting the concept of  
 816 a skin-printable hydrogel. (b) Photograph showing the attachment of Ag/AgCl  
 817 electrode to the GGW-NH<sub>4</sub>Cl hydrogel, highlighting the superior adhesion. (c)  
 818 Schematic of electrode positions for EOG signal measurements. (d) EOG signals  
 819 recorded using commercial paste (top) and the GGW-NH<sub>4</sub>Cl hydrogel (bottom), along



820 with the corresponding SNR. Reproduced with permission [180]. Copyright 2025,  
821 Elsevier. (e) Schematic illustration of the preparation, function, and application of  
822 oxidative metal ions-free lignin-catalyzed hydrogels. (f) Schematic diagram of PAA-  
823 LS-0.05 hydrogel-based bioelectrodes adhered to the skin of a volunteer's head for EOG  
824 monitoring. (g) Schematic diagram of the codable eye communication mechanism. (h)  
825 The gel electrodes detected the volunteers' eye movements, which the device  
826 interpreted as the word "FAFU". This volunteer effectively produced the outputs i)  
827 "thanks" and j) "merci" (French). Reproduced with permission [181]. Copyright 2025,  
828 Elsevier.

829  
830 The hydrogel was placed around the eyes for EOG signal monitoring, and then the  
831 signals were transmitted through a Bluetooth-enabled portable wireless module for real-  
832 time data collection. Fig. 12c illustrates representative EOG signals acquired with  
833 hydrogel-based epidermal electrodes, exhibiting pronounced periodic waveforms as the  
834 subject repeatedly shifts their gaze from side to side. Notably, the EOG signals obtained  
835 using the hydrogel epidermal electrode exhibit higher amplitude than those recorded  
836 using commercial paste. Meanwhile, the SNR (21.2 dB) of the hydrogel epidermal  
837 electrode surpasses that of the commercial paste (20.5 dB) (Fig. 12d).

838 To validate the capability of the hydrogel epidermal electrode in acquiring EOG signals  
839 from patients with speech impairments, Pan et al. reported a multifunctional PAA  
840 hydrogel catalyzed by oxidative metal-ion-free lignin<sup>181</sup>. By incorporating transition  
841 metal ions and sodium lignosulfonate (LS), LS rapidly reduces Fe<sup>3+</sup> to Fe<sup>2+</sup>, thereby  
842 promoting the rapid generation of free radicals by APS (initiator) at room temperature.  
843 This mechanism accelerates the polymerization of vinyl monomers, enabling the rapid  
844 assembly of the hydrogel (Fig. 12e). The hydrogel exhibits excellent flexibility (~7 kPa),  
845 remarkable stretchability (~2700% strain), and strong skin adhesion (~9 kPa).

846 Notably, the hydrogel, integrating these superior properties, can serve as an epidermal  
847 electrode for the human body, offering a viable alternative to conventional commercial  
848 electrodes. Fig. 12f illustrates a volunteer wearing the PAA-LS-0.05 hydrogel  
849 epidermal electrode undergoing an EOG test. The volunteer simulated a patient with  
850 severe physical and verbal impairments, retaining only limited facial skin mobility and  
851 lacking the ability to speak or type. To address this, the actions of closing the left and



852 right eyes were defined as “+” and “-”, respectively (Fig. 12g), and a reference table  
853 comprising 26 English letters and punctuation marks was developed. Through regular  
854 eye movements, the patient could achieve linguistic output and communication. As  
855 shown in Fig. 12h, the patient successfully produced the unordered sequence “F A F  
856 U” via eye movements, with the signal being clearly readable. Subsequently, the patient  
857 further expressed the English word “THANKS” (Fig. 12i) and the French word  
858 “MERCİ” (meaning “thank you”, Fig. 12j) through eye movements. This wearable  
859 hydrogel electrode seamlessly integrates with the eye-movement-based communication  
860 system, offering a significant and urgent solution to address communication challenges  
861 for such patients.

862 While conductive hydrogel-based epidermal electrodes have demonstrated excellent  
863 performance across various electrophysiological modalities—including ECG, EMG,  
864 EEG, and EOG—their practical deployment in dynamic, real-world environments  
865 poses additional challenges related to signal stability and quality. Motion artifacts  
866 remain a major concern in wearable and long-term bioelectronic monitoring, often  
867 arising from skin deformation, electrode displacement, or body movement. These  
868 artifacts can significantly distort low-amplitude biopotentials—particularly in EEG and  
869 ECG recordings—thereby compromising signal fidelity and diagnostic accuracy. The  
870 intrinsic softness, stretchability, and conformability of hydrogel-based electrodes help  
871 maintain stable skin–electrode contact, effectively minimizing impedance fluctuations  
872 and suppressing artifact generation at the source. Additionally, signal processing  
873 techniques such as adaptive filtering, baseline drift correction, and motion-sensor-  
874 assisted denoising are widely employed to further improve signal quality. Therefore,  
875 the integration of material-level optimization and algorithmic post-processing is  
876 essential for achieving reliable, high-fidelity electrophysiological recordings under  
877 real-life conditions.



## 878 **5. Summary and Perspectives**

879 Conductive hydrogels, characterized by their intrinsic flexibility, tunable properties on  
880 adhesion and electrical conductivity, hold significant promise for the development of  
881 high-performance epidermal electrodes. This review offers a comprehensive overview  
882 of recent advances in conductive hydrogel-based electrodes for electrophysiological  
883 monitoring. We first examined the underlying conductive mechanisms—ionic,  
884 electronic, and hybrid pathways—followed by a discussion of the essential properties  
885 required for effective signal acquisition, such as high conductivity, strong adhesion,  
886 stretchability, and breathability. Finally, we highlighted recent progress in their  
887 application across various electrophysiological monitoring scenarios. Despite notable  
888 achievements, several challenges persist that must be addressed to fully realize their  
889 potential.

### 890 **Advancements in materials and conductivity mechanisms**

891 The future development of conductive hydrogel-based epidermal electrodes will be  
892 driven by innovations in materials science and the continued refinement of conductivity  
893 mechanisms. While current strategies largely focus on ionic, electronic, and hybrid  
894 conduction, future research will likely prioritize optimizing these mechanisms for  
895 enhanced signal fidelity and long-term stability. Incorporating advanced conductive  
896 polymers and nanomaterials could significantly improve electronic conductivity,  
897 overcoming the environmental sensitivity associated with ionic pathways. Additionally,  
898 bioinspired designs—such as the integration of conductive peptides or materials that  
899 mimic the skin's natural electrical properties—offer the potential for improved  
900 biocompatibility and seamless integration with biological systems. These innovations  
901 aim to produce electrodes capable of reliable, high-quality electrophysiological  
902 monitoring in dynamic and diverse conditions.

### 903 **Strategies for long-term reliability**

904 Long-term performance and durability of conductive hydrogel-based epidermal





905 electrodes can be greatly enhanced through advanced materials design and interfacial  
906 engineering. One promising direction is the development of fatigue-resistant  
907 architectures, such as self-healing polymer networks and dynamic crosslinking systems,  
908 which can maintain mechanical integrity under repeated deformation. Hybrid structures  
909 that combine elastomers with hydrogels may further improve stretchability and  
910 resistance to cracking. To address adhesion challenges under real-world conditions—  
911 such as perspiration, oily skin, or continuous body motion—bioinspired adhesive  
912 strategies present an exciting pathway. These may include catechol-functionalized  
913 chemistries, microstructured surface designs, or reversible covalent bonding, enabling  
914 robust and repeatable skin contact. Advances in hydration management are also  
915 expected to play a crucial role in maintaining performance over extended use. Future  
916 studies may explore the integration of moisture-retentive additives, breathable yet  
917 protective encapsulation materials, or systems capable of autonomous hydration  
918 regulation to prevent dehydration and ion leaching.

### 919 **Multifunctionality and smart features**

920 Beyond signal monitoring, the next generation of conductive hydrogel electrodes is  
921 expected to embrace multifunctionality and smart responsiveness. One promising  
922 direction is the development of closed-loop systems, where electrodes not only detect  
923 physiological signals but also trigger therapeutic interventions, such as on-demand drug  
924 delivery. Incorporating self-healing capabilities through dynamic covalent bonds or  
925 supramolecular interactions could greatly enhance durability, especially under  
926 mechanical strain during long-term use. Additional smart features—such as energy  
927 harvesting from body movement or adaptive behavior in response to skin conditions—  
928 could further extend the functionality and lifespan of these devices. These  
929 advancements will transform conductive hydrogels into versatile, intelligent platforms  
930 that bridge sensing, therapy, and human-machine interfaces.

### 931 **Wearability, data integration, and personalized medicine**

932 The long-term vision for conductive hydrogel-based epidermal electrodes lies in their



933 seamless integration into wearable systems that support comfort, continuous data  
934 acquisition, and personalized healthcare. Innovations in material design—particularly  
935 ultrathin, breathable, and skin-conformal hydrogels—will be crucial to improving  
936 wearability and minimizing skin irritation during extended use. Simultaneously,  
937 integrating these devices with advanced data analytics and machine learning algorithms  
938 will unlock their potential for real-time monitoring, predictive diagnostics, and  
939 personalized treatment strategies. This convergence of soft materials, digital health, and  
940 precision medicine heralds a shift toward proactive, patient-centered care, where  
941 electrophysiological monitoring becomes not just reactive but a key driver in managing  
942 health and disease.

#### 943 **CRedit Authorship Contribution Statement**

944 **Jiawei Yang:** Writing – origin draft, Writing – review&editing, Investigation, Data  
945 curation. **Yi Liu:** Writing – origin draft, Writing – review&editing, Resources,  
946 Methodology, Data curation. **Wenqing Yan:** Writing – review&editing, Formal  
947 analysis. **Pengcheng Zhou:** Writing – review&editing, Formal analysis. **Zonglei**  
948 **Wang:** Writing – review&editing, Formal analysis. **Yuli Wang:** Writing –  
949 review&editing. **Yujie Zhang:** Writing – review&editing, Formal analysis. **Zongman**  
950 **Zhang:** Writing – review&editing, Software. **Fan Mo:** Writing – review&editing.  
951 **Zichong Ji:** Writing – review&editing. **Hossam Haick:** Writing – review&editing.  
952 **Yan Wang:** Writing – review&editing, Project administration, Funding acquisition,  
953 Conceptualization.

#### 954 **Declaration of Competing Interest**

955 The authors declare that they have no known competing financial interests or personal  
956 relationships that could have appeared to influence the work reported in this paper.



957 **Acknowledgments**

958 The authors sincerely acknowledge the support from the Natural Science Foundation  
959 of China (grant No.: 52303371, W2521021), Guangdong Science and Technology  
960 Department (grant Nos.: STKJ2023075, 2022A1515110209, 2021B0301030005), seed  
961 fund from GTIIT Changzhou Innovation Institute (grant No.: GCII-Seed-202406), and  
962 the Key Discipline (KD) Fund, the Technion, and the Start-Up Fund from Guangdong  
963 Technion.

964 **Notes and Reference**

- 965 1. Y. Xiang, K. Shi, Y. Li, J. Xue, Z. Tong, H. Li, Z. Li, C. Teng, J. Fang and N.  
966 Hu, *Nano-Micro Lett.*, 2024, **16**, 132.
- 967 2. J. P. Piccini, A. M. Russo, P. S. Sharma, J. Kron, W. Tzou, W. Sauer, D. S.  
968 Park, U. Birgersdotter-Green, D. S. Frankel and J. S. Healey, *Circulation:  
969 Arrhythmia and Electrophysiology*, 2022, **15**, e009911.
- 970 3. K. E. Odening, A.-M. Gomez, D. Dobrev, L. Fabritz, F. R. Heinzel, M. E.  
971 Mangoni, C. E. Molina, L. Sacconi, G. Smith and M. Stengl, *EP Europace*,  
972 2021, **23**, 1795-1814.
- 973 4. A. H. Caillet, A. T. Phillips, L. Modenese and D. Farina, *J. Electromyogr.  
974 Kinesiol.*, 2024, **76**, 102873.
- 975 5. R. Sun, A. Sohrabpour, G. A. Worrell and B. He, *PNAS*, 2022, **119**,  
976 e2201128119.
- 977 6. F. Arcuri, C. Porcaro, I. Ciancarelli, P. Tonin and A. Cerasa, *Electronics*, 2021,  
978 **10**, 836.
- 979 7. M. Pyasik, M. Scandola and V. Moro, *Neuropsychologia*, 2022, **174**, 108333.
- 980 8. C.-l. a. R. Labs, D. Sussillo, P. Kaifosh and T. Reardon, *Biorxiv*, 2024,  
981 2024.2002.2023.581779.
- 982 9. H. Zhang, D. Zhang, Z. Wang, G. Xi, R. Mao, Y. Ma, D. Wang, M. Tang, Z.  
983 Xu and H. Luan, *ACS Appl. Mater. Interfaces*, 2023, **15**, 5128-5138.
- 984 10. J. W. Kam, T. Rahnuma, Y. Park and C. Hart, *Neuroimage*, 2022, **258**, 119372.
- 985 11. M. Zhu, H. Wang, S. Li, X. Liang, M. Zhang, X. Dai and Y. Zhang, *Adv.  
986 Healthcare Mater.*, 2021, **10**, 2100646.
- 987 12. Y. Luo, W. Li, Q. Lin, F. Zhang, K. He, D. Yang, X. J. Loh and X. Chen, *Adv.  
988 Mater.*, 2021, **33**, 2007848.
- 989 13. P. Kateb, J. Fan, J. Kim, X. Zhou, G. A. Lodygensky and F. Cicoira, *Flexible  
990 Printed Electron.*, 2023, **8**, 045006.



- 991 14. J. Kim, J. Fan, G. Petrossian, X. Zhou, P. Kateb, N. Gagnon-Lafrenais and F. Cicoira, *Mater. Horiz.*, 2024, **11**, 3548-3560.
- 992
- 993 15. X. Zhou, P. Kateb, J. Fan, J. Kim, G. A. Lodygensky, B. Amilhon, D. Pasini and F. Cicoira, *J. Mater. Chem. C*, 2024, **12**, 5708-5717.
- 994
- 995 16. F. Han, X. Huang and E. Teye, *J. Food Process Eng.*, 2019, **42**, e12983.
- 996 17. Q. Ouyang, Y. Yang, J. Wu, Q. Chen, Z. Guo and H. Li, *Lwt*, 2020, **118**, 108768.
- 997 18. W. Zhang, C. Liu, F. Liu, X. Zou, Y. Xu and X. Xu, *Food Chem.*, 2020, **303**, 125378.
- 998
- 999 19. B. Lu, F. Han, J. H. Aheto, M. M. Rashed and Z. Pan, *Food Science & Nutrition*, 2021, **9**, 5220-5228.
- 1000
- 1001 20. H. Yin, X. Hu, X. Huang, X. Zou, Y. Xu, J. Shi and M. Yang, *Food Anal. Methods*, 2021, **14**, 1836-1842.
- 1002
- 1003 21. S. Yang and X. Jiang, *ACS Nano*, 2024, **18**, 27107-27125.
- 1004 22. H. Ullah, M. A. Wahab, G. Will, M. R. Karim, T. Pan, M. Gao, D. Lai, Y. Lin and M. H. Miraz, *Biosensors*, 2022, **12**, 630.
- 1005
- 1006 23. J. Yi, Y. Gu, J. Yang, Z. Wang, Y. Wang, W. Yan, Q. Sun, P. Zhou, Y. Xu, X. He, J. Zhong and Y. Wang, *Mater. Horiz.*, 2025, DOI: 10.1039/D4MH01858C.
- 1007
- 1008 24. J. Yang, Q. Sun, Z. Wang, Y. Xu, Y. Wang, W. Yan, P. Zhou, Z. Ji, H. Jiang, S. Chen, W. Zhang, H. Haick and Y. Wang, *Wearable Electronics*, 2025, **2**, 55-61.
- 1009
- 1010
- 1011 25. H. Wu, G. Yang, K. Zhu, S. Liu, W. Guo, Z. Jiang and Z. Li, *Adv. Sci.*, 2021, **8**, 2001938.
- 1012
- 1013 26. L. Hu, P. L. Chee, S. Sugiarto, Y. Yu, C. Shi, R. Yan, Z. Yao, X. Shi, J. Zhi and D. Kai, *Adv. Mater.*, 2023, **35**, 2205326.
- 1014
- 1015 27. L. Wang, T. Xu and X. Zhang, *TrAC Trends Anal. Chem.*, 2021, **134**, 116130.
- 1016 28. M. L. Oyen, *Int. Mater. Rev.*, 2014, **59**, 44-59.
- 1017 29. E. M. Ahmed, *J. Adv. Res.*, 2015, **6**, 105-121.
- 1018 30. H. Yuk, B. Lu and X. Zhao, *Chem. Soc. Rev.*, 2019, **48**, 1642-1667.
- 1019 31. Y. Zhao, X. Fu, B. Liu, J. Sun, Z. Zhuang, P. Yang, J. Zhong and K. Liu, *Sci. China. Mater.*, 2023, **66**, 1934-1940.
- 1020
- 1021 32. F. Mo, P. Zhou, S. Lin, J. Zhong and Y. Wang, *Adv. Healthcare Mater.*, 2024, **13**, 2401503.
- 1022
- 1023 33. Y. Huang, M. Xiao, X. Zhou, J. Zhu, Y. Tian, S. Xie, Y. Gong and J. Zhong, *Sens. Actuators B Chem.*, 2025, **431**, 137461.
- 1024
- 1025 34. Y. Liu, L. Han, S. Lv, T. Jiang, M. Duan, H. Guo, Y. Li, Q. Xie, Y. Chen and D. Wang, *Research*, 2025, **8**, 0714.
- 1026
- 1027 35. Y. Zhou, Y. Zhao, D. Zhao, X. Guan, K. Zhang, Y. Pi and J. Zhong, *Microsyst. Nanoeng.*, 2025, **11**, 40.
- 1028
- 1029 36. K. Deligkaris, T. S. Tadele, W. Olthuis and A. van den Berg, *Sens. Actuators B Chem.*, 2010, **147**, 765-774.
- 1030
- 1031 37. Y. S. Zhang and A. Khademhosseini, *Science*, 2017, **356**, eaaf3627.
- 1032 38. P. Zhou, F. Mo, Z. Ji, J. Yang, H. Du, Z. Wang, H. Haick and Y. Wang, *Sci.*



- 1033 *Bull.*, 2025, DOI: <https://doi.org/10.1016/j.scib.2025.01.058>.
- 1034 39. F. Mo, P. Zhou, S. Lin, J. Zhong and Y. Wang, *Adv. Healthcare Mater.*, 2024,  
1035 **13**, 2401503.
- 1036 40. P. Zhou, Z. Zhang, F. Mo and Y. Wang, *Adv. Sens. Res.*, 2024, **3**, 2300021.
- 1037 41. F. Mo, Y. Lin, Y. Liu, P. Zhou, J. Yang, Z. Ji and Y. Wang, *Mater. Sci. Eng. R*  
1038 *Rep.*, 2025, **165**, 100989.
- 1039 42. M. Niu, K. Chen, W. Li, J. Hu, J. Zhang, P. Zhu, Z. Pan and Y. Mao, *J. Mater.*  
1040 *Res.*, 2024, **39**, 188-211.
- 1041 43. H. Duan, Y. Zhang, Y. Zhang, P. Zhu and Y. Mao, *Nanomaterials*, 2024, **14**,  
1042 1398.
- 1043 44. W. Hu, D. Song, X. Shi and N. Liu, *SCIENTIA SINICA Chimica*, 2022, **52**, 837-  
1044 847.
- 1045 45. H. Ding, Y. Gu, Y. Ren, C. Hu, Q. Qiu, D. Wu, J. Mou, Z. Wu and H. Zhou, *J.*  
1046 *Mater. Chem. C*, 2024.
- 1047 46. Q. Han, C. Zhang, T. Guo, Y. Tian, W. Song, J. Lei, Q. Li, A. Wang, M. Zhang,  
1048 S. Bai and X. Yan, *Adv. Mater.*, 2023, **35**, 2209606.
- 1049 47. Q. Han, X. Gao, C. Zhang, Y. Tian, S. Liang, X. Li, Y. Jing, M. Zhang, A. Wang  
1050 and S. Bai, *Adv. Mater.*, 2025, **37**, 2415445.
- 1051 48. Y. Li, Y. Gu, S. Qian, S. Zheng, Y. Pang, L. Wang, B. Liu, S. Liu and Q. Zhao,  
1052 *Nano Res.*, 2024, **17**, 5479-5490.
- 1053 49. Z. Zhang, J. Yang, H. Wang, C. Wang, Y. Gu, Y. Xu, S. Lee, T. Yokota, H.  
1054 Haick, T. Someya and Y. Wang, *Sci. Adv.*, 2024, **10**, eadj5389.
- 1055 50. T.-C. Ho, C.-C. Chang, H.-P. Chan, T.-W. Chung, C.-W. Shu, K.-P. Chuang,  
1056 T.-H. Duh, M.-H. Yang and Y.-C. Tyan, *Molecules*, 2022, **27**, 2902.
- 1057 51. T. Zhu, Y. Ni, G. M. Biesold, Y. Cheng, M. Ge, H. Li, J. Huang, Z. Lin and Y.  
1058 Lai, *Chem. Soc. Rev.*, 2023, **52**, 473-509.
- 1059 52. H. Dechiraju, M. Jia, L. Luo and M. Rolandi, *Adv. Sustain. Syst.*, 2022, **6**,  
1060 2100173.
- 1061 53. S. Chen, Y. Chen, X. Mu, P. Wang, L. Miao, S. Tanemura and H. Cai, *Sustain.*  
1062 *Mater. Technol.*, 2023, **36**, e00635.
- 1063 54. X. Li, Y. Sun, S. Wang, G. Tian, T. Yang, L. Huang, Y. Ao, B. Lan, J. Zhang,  
1064 T. Xu, Y. Liu, L. Jin, W. Yang and W. Deng, *Chem. Eng. J.*, 2024, **498**, 155195.
- 1065 55. C. G. Wang, N. E. B. Surat'man, J. J. Chang, Z. L. Ong, B. Li, X. Fan, X. J. Loh  
1066 and Z. Li, *Chemistry—An Asian Journal*, 2022, **17**, e202200604.
- 1067 56. A. S. Ivanov, L. V. Pershina, K. G. Nikolaev and E. V. Skorb, *Macromol.*  
1068 *Biosci.*, 2021, **21**, 2100117.
- 1069 57. D. Lu, Z. Zhu, M. Zhu, P. Zhang and X. Xiang, *J. Mater. Chem. A*, 2025, **13**,  
1070 427-440.
- 1071 58. Y. Gao, W. Zhang, L. Li, Z. Wang, Y. Shu and J. Wang, *Chem. Eng. J.*, 2023,  
1072 **452**, 139248.
- 1073 59. Z. Luo, W. Li, J. Yan and J. Sun, *Adv. Funct. Mater.*, 2022, **32**, 2203988.
- 1074 60. Y. Zhao, F. Wang, J. Liu, D. Gan, B. Lei, J. Shao, W. Wang, Q. Wang and X.

View Article Online  
DOI: 10.1039/D5TC01896J



- 1075 Dong, *ACS Appl. Mater. Interfaces*, 2023, **15**, 28664-28674.
- 1076 61. Q. He, Y. Cheng, Y. Deng, F. Wen, Y. Lai and H. Li, *Adv. Funct. Mater.*, 2024,  
1077 **34**, 2308974.
- 1078 62. F. Miguel, F. Barbosa, F. C. Ferreira and J. C. Silva, *Gels*, 2022, **8**, 710.
- 1079 63. M. A. Bhat, R. A. Rather and A. H. Shalla, *Synth. Met.*, 2021, **273**, 116709.
- 1080 64. B. Zhao, Z. Li, L. Zheng, Z. Ye, Y. Yuan, S. Zhang, B. Liang and T. Li, *Chin.*  
1081 *Chem. Lett.*, 2024, **35**, 109810.
- 1082 65. R. Eivazzadeh-Keihan, E. B. Noruzi, E. Chidar, M. Jafari, F. Davoodi, A.  
1083 Kashtiaray, M. G. Gorab, S. M. Hashemi, S. Javanshir and R. A. Cohan, *Chem.*  
1084 *Eng. J.*, 2022, **442**, 136183.
- 1085 66. R. Arambula-Maldonado and K. Mequanint, *Materials Advances*, 2022, **3**,  
1086 5186-5206.
- 1087 67. Y. Zhao, K. Zhao, R. Qian, Z. Yu and C. Ye, *Chem. Eng. J.*, 2024, 150197.
- 1088 68. Y. Wang, M. Zhang, Z. Yan, S. Ji, S. Xiao and J. Gao, *Theranostics*, 2024, **14**,  
1089 1534.
- 1090 69. X. Huang, C. Chen, X. Ma, T. Zhu, W. Ma, Q. Jin, R. Du, Y. Cai, M. Zhang, D.  
1091 Kong, M. Wang, J. a. Ren, Q. Zhang and X. Jia, *Adv. Funct. Mater.*, 2023, **33**,  
1092 2302846.
- 1093 70. J. Dai, D. Ren, S. Zhang, Y. Liu, Y. Xiao, Z. Wang, B. Wang and F. Huang,  
1094 *ACS Appl. Electron. Mater.*, 2025, **7**, 3125-3134.
- 1095 71. Y. Ohm, C. Pan, M. J. Ford, X. Huang, J. Liao and C. Majidi, *Nat. Electron.*,  
1096 2021, **4**, 185-192.
- 1097 72. J. Chen, F. Liu, T. Abdiryim and X. Liu, *Adv. Compos. Hybrid Mater.*, 2024, **7**,  
1098 35.
- 1099 73. J. Luo, C. Sun, B. Chang, Y. Jing, K. Li, Y. Li, Q. Zhang, H. Wang and C. Hou,  
1100 *ACS Nano*, 2022, **16**, 19373-19384.
- 1101 74. C. Yu, Z. Yue, H. Zhang, M. Shi, M. Yao, Q. Yu, M. Liu, B. Guo, H. Zhang, L.  
1102 Tian, H. Sun, F. Yao and J. Li, *Adv. Funct. Mater.*, 2023, **33**, 2211023.
- 1103 75. P. Wang, Y. Lv, J. Duan, G. Sun, C. Meng, Y. Li, S. Guo and T. Zhang, *Nano*  
1104 *Energy*, 2025, **136**, 110722.
- 1105 76. F. Wang, L. Yang, Y. Sun, Y. Cai, X. Xu, Z. Liu, Q. Liu, H. Zhao, C. Ma and  
1106 J. Liu, *Gels*, 2023, **9**, 323.
- 1107 77. Z. Wang, L. Chen, Y. Chen, P. Liu, H. Duan and P. Cheng, *Research*, 2020,  
1108 **2020**.
- 1109 78. Y. Liu, C. Wang, J. Xue, G. Huang, S. Zheng, K. Zhao, J. Huang, Y. Wang, Y.  
1110 Zhang and T. Yin, *Adv. Healthcare Mater.*, 2022, **11**, 2270092.
- 1111 79. L. Rong, X. Xie, W. Yuan and Y. Fu, *ACS Appl. Mater. Interfaces*, 2022, **14**,  
1112 29273-29283.
- 1113 80. Y. Shi, Y. Ding, W. Wang and D. Yu, *Colloids and Surfaces A:*  
1114 *Physicochemical and Engineering Aspects*, 2023, **675**, 132081.
- 1115 81. R. Liu, T. Wang, G. Li, Z. Fan, Q. Zhou, K. Wang, P. Li and W. Huang, *Adv.*  
1116 *Funct. Mater.*, 2023, **33**, 2214917.



- 1117 82. Q. Liang, X. Xia, X. Sun, D. Yu, X. Huang, G. Han, S. M. Mugo, W. Chen and  
1118 Q. Zhang, *Adv. Sci.*, 2022, **9**, 2201059.
- 1119 83. Q. Wu, A. Chen, Y. Xu, S. Han, J. Zhang, Y. Chen, J. Hang, X. Yang and L.  
1120 Guan, *Soft Matter*, 2024, **20**, 3666-3675.
- 1121 84. X. Pan, Q. Wang, P. He, K. Liu, Y. Ni, X. Ouyang, L. Chen, L. Huang, H. Wang  
1122 and Y. Tan, *ACS Sustain. Chem. Eng.*, 2019, **7**, 7918-7925.
- 1123 85. M. Lu, L. Shen, H. Su, B. Li, L. Wang and W. W. Yu, *J. Colloid Interface Sci.*,  
1124 2025, **684**, 272-282.
- 1125 86. H. Ma, J. Hou, X. Xiao, R. Wan, G. Ge, W. Zheng, C. Chen, J. Cao, J. Wang,  
1126 C. Liu, Q. Zhao, Z. Zhang, P. Jiang, S. Chen, W. Xiong, J. Xu and B. Lu, *J.*  
1127 *Colloid Interface Sci.*, 2024, **654**, 639-648.
- 1128 87. J. Lao, Y. Jiao, Y. Zhang, H. Xu, Y. Wang, Y. Ma, X. Feng and J. Yu, *ACS*  
1129 *Nano*, 2025, **19**, 7755-7766.
- 1130 88. J. Zheng, J. Zhou, Y. Zhao, C. Wang, M. Fan, Y. Li, C. Yang and H. Yang,  
1131 *Biosensors*, 2025, **15**, 177.
- 1132 89. X. Xia, Q. Liang, X. Sun, D. Yu, X. Huang, S. M. Mugo, W. Chen, D. Wang  
1133 and Q. Zhang, *Adv. Funct. Mater.*, 2022, **32**, 2208024.
- 1134 90. H. Xue, D. Wang, M. Jin, H. Gao, X. Wang, L. Xia, D. a. Li, K. Sun, H. Wang,  
1135 X. Dong, C. Zhang, F. Cong and J. Lin, *Microsyst. Nanoeng.*, 2023, **9**, 79.
- 1136 91. N. Li, X. Wang, Y. Liu, Y. Li, J. Li, Z. Qin and T. Jiao, *Chem. Eng. J.*, 2024,  
1137 **483**, 149303.
- 1138 92. J. Wei, H. Chen, F. Pan, H. Zhang, K. Yang, T. Yuan, Y. Fang, H. Ping, Q.  
1139 Wang and Z. Fu, *ACS Nano*, 2025, **19**, 15554-15564.
- 1140 93. X. Zhou, A. Rajeev, A. Subramanian, Y. Li, N. Rossetti, G. Natale, G. A.  
1141 Lodygensky and F. Cicoira, *Acta Biomater.*, 2022, **139**, 296-306.
- 1142 94. H. Huang, J. Shen, S. Wan, L. Han, G. Dou and L. Sun, *ACS Appl. Mater.*  
1143 *Interfaces*, 2023, **15**, 11549-11562.
- 1144 95. D. Kim, H. J. Lee, J. Oh, H. Y. Yang, H. J. Park, C. Huh, D. H. Ha, Y. Jun and  
1145 Y. J. Yun, *J. Mater. Chem. C*, 2025, **13**, 5711-5718.
- 1146 96. M. Li, W. Li, Q. Guan, J. Lv, Z. Wang, L. Ding, C. Li, E. Saiz and X. Hou,  
1147 *Device*, 2023, **1**.
- 1148 97. H. Su, L. Mao, X. Chen, P. Liu, J. Pu, Z. Mao, T. Fujiwara, Y. Ma, X. Mao and  
1149 T. Li, *Adv. Sci.*, 2024, **11**, 2405273.
- 1150 98. B. Yao, Y. Yan, Q. Cui, S. Duan, C. Wang, Y. Du, Y. Zhao, D. Wu, S. Wu, X.  
1151 Zhu, T. Hsiai and X. He, *Matter*, 2022, **5**, 4407-4424.
- 1152 99. C. Liu, Y. Wang, S. Shi, Y. Zheng, Z. Ye, J. Liao, Q. Sun, B. Dang and X. Shen,  
1153 *ACS Nano*, 2024, **18**, 27420-27432.
- 1154 100. H. He, H. Li, A. Pu, W. Li, K. Ban and L. Xu, *Nat. Commun.*, 2023, **14**, 759.
- 1155 101. J. Zhang, Y. Wang, Q. Wei, Y. Wang, M. Lei, M. Li, D. Li, L. Zhang and Y.  
1156 Wu, *Gels*, 2021, **7**, 216.
- 1157 102. Z. Chen, Y. Chen, M. S. Hedenqvist, C. Chen, C. Cai, H. Li, H. Liu and J. Fu,  
1158 *J. Mater. Chem. B*, 2021, **9**, 2561-2583.

View Article Online  
DOI: 10.1039/D5TC01896J



- 1159 103. W. Li, J. Liu, J. Wei, Z. Yang, C. Ren and B. Li, *Adv. Funct. Mater.*, 2023, **33**, 2213485. View Article Online  
DOI: 10.1039/D3TC01896J
- 1160
- 1161 104. J. Zhang, Y. Hu, L. Zhang, J. Zhou and A. Lu, *Nano-Micro Lett.*, 2022, **15**, 8.
- 1162 105. G. Kougkoulos, M. Golzio, L. Laudebat, Z. Valdez-Nava and E. Flahaut, *J.*
- 1163 *Mater. Chem. B*, 2023, **11**, 2036-2062.
- 1164 106. L. Li, J. Meng, M. Zhang, T. Liu and C. Zhang, *Chem. Commun. (Cambridge,*
- 1165 *U. K.)*, 2022, **58**, 185-207.
- 1166 107. Z. Wang, X. Xu, R. Tan, S. Zhang, K. Zhang and J. Hu, *Adv. Funct. Mater.*,
- 1167 2024, **34**, 2312667.
- 1168 108. Q. Zhang, H. Lu, G. Yun, L. Gong, Z. Chen, S. Jin, H. Du, Z. Jiang and W. Li,
- 1169 *Adv. Funct. Mater.*, 2024, **34**, 2308113.
- 1170 109. S. Li, Y. Cong and J. Fu, *J. Mater. Chem. B*, 2021, **9**, 4423-4443.
- 1171 110. X. Ma, X. Zhou, J. Ding, B. Huang, P. Wang, Y. Zhao, Q. Mu, S. Zhang, C.
- 1172 Ren and W. Xu, *J. Mater. Chem. A*, 2022, **10**, 11823-11853.
- 1173 111. X. Shi and P. Wu, *Small*, 2021, **17**, 2101220.
- 1174 112. X. Shi and P. Wu, *Small*, 2021, **17**, 2101220.
- 1175 113. Y. Gao, K. Wu and Z. Suo, *Adv. Mater.*, 2019, **31**, 1806948.
- 1176 114. T. Wang, P. Zhang, X. Yang, Y. Zhang, J. Zhang, X. He, P. Gu, X. Gong and
- 1177 Y. Zhao, *Chem. Eng. J.*, 2022, **438**, 135441.
- 1178 115. Z. Xu, X. Liang, W. Ma, X. An, H. Wu, Q. Zhang and X. Jia, *Adv. Funct. Mater.*,
- 1179 2024, **34**, 2310233.
- 1180 116. Y. Liu, P. Wang, X. Su, L. Xu, Z. Tian, H. Wang, G. Ji and J. Huang, *Adv.*
- 1181 *Mater.*, 2022, **34**, 2108820.
- 1182 117. G. Bovone, O. Y. Dudaryeva, B. Marco-Dufort and M. W. Tibbitt, *ACS*
- 1183 *Biomater. Sci. Eng.*, 2021, **7**, 4048-4076.
- 1184 118. Y. Zhao, S. Song, X. Ren, J. Zhang, Q. Lin and Y. Zhao, *Chem. Rev.*, 2022,
- 1185 **122**, 5604-5640.
- 1186 119. Y.-W. Lee, S. Chun, D. Son, X. Hu, M. Schneider and M. Sitti, *Adv. Mater.*,
- 1187 2022, **34**, 2109325.
- 1188 120. L. Nicolle, C. M. Journot and S. Gerber-Lemaire, *Polymers*, 2021, **13**, 4118.
- 1189 121. W. Zhang, Y. Zhang, Y. Zhang, Y. Dai, F. Xia and X. Zhang, *J. Mater. Chem.*
- 1190 *B*, 2021, **9**, 5954-5966.
- 1191 122. X. Wei, Y. Wang, Y. Liu, K. Ji, K. Li, J. Wang and Z. Gu, *Matter*, 2024, **7**, 826-
- 1192 854.
- 1193 123. S. Jia, T. Tao, J. Sun, J. Du, Y. Xie, L. Yu, W. Tang, J. Wang and J. Gong,
- 1194 *Small Structures*, 2023, **4**, 2300139.
- 1195 124. G. Giordano, M. Carlotti and B. Mazzolai, *Adv. Mater. Technol.*, 2021, **6**,
- 1196 2100437.
- 1197 125. T. Cheng, Y. Z. Zhang, S. Wang, Y. L. Chen, S. Y. Gao, F. Wang, W. Y. Lai
- 1198 and W. Huang, *Adv. Funct. Mater.*, 2021, **31**, 2101303.
- 1199 126. Y. Zhang, X. Sun, Y. Ye, H. Oguzlu, Y. Zhu, J. Zhu, K. Le, P. Yang and F.
- 1200 Jiang, *Mater. Today*, 2024, **74**, 67-76.





- 1201 127. W. Li, S. Zheng, X. Zou, Y. Ren, Z. Liu, W. Peng, X. Wang, D. Liu, Z. Shen, Y. Hu, J. Guo, Z. Sun and F. Yan, *Adv. Funct. Mater.*, 2022, **32**, 2207348. View Article Online  
DOI: 10.1039/D5TC01896J
- 1202
- 1203 128. R. Ji, S. Yan, Z. Zhu, Y. Wang, D. He, K. Wang, D. Zhou, Q. Jia, X. Wang, B. Zhang, C. Shi, T. Xu, R. Wang, R. Wang and Y. Zhou, *Adv. Sci.*, 2024, **11**, 2401869.
- 1204
- 1205
- 1206 129. J. Yang, Z. Zhang, P. Zhou, Y. Zhang, Y. Liu, Y. Xu, Y. Gu, S. Qin, H. Haick and Y. Wang, *Nanoscale*, 2023, **15**, 3051-3078.
- 1207
- 1208 130. Y. Wang, *Soft Sci*, 2024, **4**.
- 1209 131. Y. Wang, H. Haick, S. Guo, C. Wang, S. Lee, T. Yokota and T. Someya, *Chem. Soc. Rev.*, 2022, **51**, 3759-3793.
- 1210
- 1211 132. S. Cheng, Z. Lou, L. Zhang, H. Guo, Z. Wang, C. Guo, K. Fukuda, S. Ma, G. Wang, T. Someya, H.-M. Cheng and X. Xu, *Adv. Mater.*, 2023, **35**, 2206793.
- 1212
- 1213 133. S. Wei, R. Yin, T. Tang, Y. Wu, Y. Liu, P. Wang, K. Wang, M. Mei, R. Zou and X. Duan, *ACS Nano*, 2019, **13**, 7920-7929.
- 1214
- 1215 134. B. Khan, Z. Riaz and B. L. Khoo, *Mater. Sci. Eng. R Rep.*, 2024, **159**, 100804.
- 1216 135. P. A. Moreno-Sánchez, G. García-Isla, V. D. Corino, A. Vehkaoja, K. Brukamp, M. Van Gils and L. Mainardi, *Comput. Biol. Med.*, 2024, 108235.
- 1217
- 1218 136. J. C. Hwang, M. Kim, S. Kim, H. Seo, S. An, E. H. Jang, S. Y. Han, M. J. Kim, N. K. Kim and S.-W. Cho, *Sci. Adv.*, 2022, **8**, eabq0897.
- 1219
- 1220 137. S.-H. Sunwoo, S. I. Han, C. S. Park, J. H. Kim, J. S. Georgiou, S.-P. Lee, D.-H. Kim and T. Hyeon, *Nat. Rev. Bioeng.*, 2024, **2**, 8-24.
- 1221
- 1222 138. B. Pan, F. Xiong, J. Wang, J. Fu, Y. Ding, R. Qin and S. Li, *Talanta*, 2025, 127591.
- 1223
- 1224 139. Y. Du, J. H. Kim, H. Kong, A. A. Li, M. L. Jin, D. H. Kim and Y. Wang, *Adv. Healthcare Mater.*, 2024, **13**, 2303461.
- 1225
- 1226 140. S. Tang, D. Sha, Z. He, X. Chen, Y. Ma, C. Liu and Y. Yuan, *Adv. Healthcare Mater.*, 2023, **12**, 2300475.
- 1227
- 1228 141. Y. Zhang, Q. Tang, J. Zhou, C. Zhao, J. Li and H. Wang, *ACS Biomater. Sci. Eng.*, 2023, **10**, 191-218.
- 1229
- 1230 142. X. Shi, H. Yu, Z. Tang, S. Lu, M. You, H. Yin and Q. Chen, *Sci. China Technol. Sci.*, 2024, **67**, 3136-3151.
- 1231
- 1232 143. G. Yang, Z. Lan, H. Gong, J. Wen, B. Pang, Y. Qiu, Y. Zhang, W. Guo, T. Bu, B. Xie and H. Wu, *Adv. Funct. Mater.*, 2025, **35**, 2417841.
- 1233
- 1234 144. S. Chen, Q. Ouyang, X. Meng, Y. Yang, C. Li, X. Miao, Z. Chen, G. Zhao, Y. Lei, B. Ghanem, S. Gautam, J. Cheng and Z. Yan, *Sci. Adv.*, 2025, **11**, eadv2406.
- 1235
- 1236 145. D. Farina, R. Merletti and R. M. Enoka, *J. Appl. Physiol.*, 2004, **96**, 1486-1495.
- 1237 146. H. Wang, Q. Ding, Y. Luo, Z. Wu, J. Yu, H. Chen, Y. Zhou, H. Zhang, K. Tao and X. Chen, *Adv. Mater.*, 2024, **36**, 2309868.
- 1238
- 1239 147. S. Yang, J. Cheng, J. Shang, C. Hang, J. Qi, L. Zhong, Q. Rao, L. He, C. Liu and L. Ding, *Nat. Commun.*, 2023, **14**, 6494.
- 1240
- 1241 148. J. Wu, J. Xian, C. He, H. Lin, J. Li and F. Li, *Adv. Mater.*, 2024, **36**, 2405372.
- 1242 149. Y. Zhang, L. Chen, M. Xie, Z. Zhan, D. Yang, P. Cheng, H. Duan, Q. Ge and



- 1243 Z. Wang, *Mater. Today Phys.*, 2022, **27**, 100794.
- 1244 150. J. Park, Y. Lee, S. Cho, A. Choe, J. Yeom, Y. G. Ro, J. Kim, D.-h. Kang, S. Lee  
1245 and H. Ko, *Chem. Rev.*, 2024, **124**, 1464-1534.
- 1246 151. H. Yuk, J. Wu and X. Zhao, *Nature Reviews Materials*, 2022, **7**, 935-952.
- 1247 152. J.-W. Lee, M.-J. Shin, M.-H. Jang, W.-B. Jeong and S.-J. Ahn, *Med. Eng. Phys.*,  
1248 2021, **98**, 65-72.
- 1249 153. V. Alcan and M. Zinnuroğlu, *Turkish journal of medical sciences*, 2023, **53**,  
1250 1019-1031.
- 1251 154. Q. Liu, X. Xu, Y. Zhang, L. Liang, B. Zhang and S. Chen, *Chem. Eng. J.*, 2025,  
1252 **509**, 161207.
- 1253 155. S. Roubert Martinez, P. Le Floch, J. Liu and R. D. Howe, *Adv. Healthcare*  
1254 *Mater.*, 2023, **12**, 2202661.
- 1255 156. R. Wan, J. Yu, Z. Quan, H. Ma, J. Li, F. Tian, W. Wang, Y. Sun, J. Liu and D.  
1256 Gao, *Chem. Eng. J.*, 2024, **490**, 151454.
- 1257 157. R. Wan, S. Liu, Z. Li, G. Li, H. Li, J. Li, J. Xu and X. Liu, *J. Colloid Interface*  
1258 *Sci.*, 2025, **677**, 198-207.
- 1259 158. T. Li, H. Qi, C. Zhao, Z. Li, W. Zhou, G. Li, H. Zhuo and W. Zhai, *Nat.*  
1260 *Commun.*, 2025, **16**, 88.
- 1261 159. J. Gavvala, N. Abend, S. LaRoche, C. Hahn, S. T. Herman, J. Claassen, M.  
1262 Macken, S. Schuele, E. Gerard and C. C. E. M. R. Consortium, *Epilepsia*, 2014,  
1263 **55**, 1864-1871.
- 1264 160. C. De Gans, P. Burger, E. Van den Ende, J. Hermanides, P. Nanayakkara, R.  
1265 Gemke, F. Rutters and D. Stenvers, *Sleep Med. Rev.*, 2024, 101951.
- 1266 161. M. Mohamed, N. Mohamed and J. G. Kim, *Biosensors*, 2023, **13**, 1019.
- 1267 162. J.-C. Hsieh, W. He, D. Venkatraghavan, V. B. Koptelova, Z. J. Ahmad, I.  
1268 Pyatnitskiy, W. Wang, J. Jeong, K. K. W. Tang and C. Harmeier, *Device*, 2024,  
1269 **2**.
- 1270 163. X. Li, Y. Zhang, P. Tiwari, D. Song, B. Hu, M. Yang, Z. Zhao, N. Kumar and  
1271 P. Marttinen, *ACM Computing Surveys*, 2022, **55**, 1-57.
- 1272 164. G. Yang, K. Zhu, W. Guo, D. Wu, X. Quan, X. Huang, S. Liu, Y. Li, H. Fang  
1273 and Y. Qiu, *Adv. Funct. Mater.*, 2022, **32**, 2200457.
- 1274 165. M. Hu, J. Ren, Y. Pan, L. Cheng, X. Xu, C. L. Tan, H. Sun, Y. Shi and S. Yan,  
1275 *Adv. Funct. Mater.*, 2024, **34**, 2407926.
- 1276 166. G. Li, Y. Liu, Y. Chen, M. Li, J. Song, K. Li, Y. Zhang, L. Hu, X. Qi and X.  
1277 Wan, *J. Neural Eng.*, 2023, **20**, 026017.
- 1278 167. J. Liu, S. Lin, W. Li, Y. Zhao, D. Liu, Z. He, D. Wang, M. Lei, B. Hong and H.  
1279 Wu, *Research*, 2022.
- 1280 168. W. U. Khan, Z. Shen, S. M. Mugo, H. Wang and Q. Zhang, *Chem. Soc. Rev.*,  
1281 2025, **54**, 2832-2880.
- 1282 169. Q. Han, C. Zhang, T. Guo, Y. Tian, W. Song, J. Lei, Q. Li, A. Wang, M. Zhang  
1283 and S. Bai, *Adv. Mater.*, 2023, **35**, 2209606.
- 1284 170. C. Wang, H. Wang, B. Wang, H. Miyata, Y. Wang, M. O. G. Nayeem, J. J. Kim,



- 1285 S. Lee, T. Yokota, H. Onodera and T. Someya, *Sci. Adv.*, 2022, **8**, eabo1396. View Article Online  
DOI: 10.1039/D5TC01896J
- 1286 171. L. Li, X. Ye, Z. Ji, M. Zheng, S. Lin, M. Wang, J. Yang, P. Zhou, Z. Zhang, B.  
1287 Wang, H. Wang and Y. Wang, *Small*, 2025, **21**, 2407996.
- 1288 172. G. Fang, X. Yang, Q. Wang, A. Zhang and B. Tang, *Materials Science and*  
1289 *Engineering: C*, 2021, **127**, 112212.
- 1290 173. R. Lev and D. Seliktar, *J. Royal Soc. Interface*, 2018, **15**, 20170380.
- 1291 174. N. A. Alba, R. J. Sclabassi, M. Sun and X. T. Cui, *IEEE Trans. Neural Syst.*  
1292 *Rehabil. Eng.*, 2010, **18**, 415-423.
- 1293 175. J. S. Blasco, E. Iáñez, A. Ubeda and J. M. Azorín, *Expert Systems with*  
1294 *Applications*, 2012, **39**, 7908-7918.
- 1295 176. G. Perale, F. Rossi, E. Sundstrom, S. Bacchiega, M. Masi, G. Forloni and P.  
1296 Veglianesi, *ACS Chem. Neurosci.*, 2011, **2**, 336-345.
- 1297 177. K. Pradhan, G. Das, J. Khan, V. Gupta, S. Barman, A. Adak and S. Ghosh,  
1298 *ACS Chem. Neurosci.*, 2018, **10**, 1535-1543.
- 1299 178. V. Martínez-Cagigal, J. Thielen, E. Santamaria-Vazquez, S. Pérez-Velasco, P.  
1300 Desain and R. Hornero, *J. Neural Eng.*, 2021, **18**, 061002.
- 1301 179. J. Sosulski and M. Tangermann, *J. Neural Eng.*, 2022, **19**, 066001.
- 1302 180. M. Zheng, L. Li, X. Ye, Z. Ji, Y. Wang, Z. Wang, S. Lin, M. Wang, W. Yan, J.  
1303 Yang, P. Zhou, Y. Zhang, R. Niu, H. Haick and Y. Wang, *Chem. Eng. J.*, 2025,  
1304 **512**, 162451.
- 1305 181. X. Pan, J. Guan, S. Cao, X. Ma, Y. Ni and Q. Wang, *J. Colloid Interface Sci.*,  
1306 2025, **680**, 753-761.
- 1307



## Data availability

The data that support the findings of this study are available from the corresponding author upon reasonable request.

